Dropwise and liquid-jet laminar flow of subcooled water falling over horizontal tube banks

Singh, Navdeep Sangeet; Stafford, Jason; Gao, Nan

DOI:
10.1016/j.ijheatmasstransfer.2023.123936

Document Version
Publisher's PDF, also known as Version of record

Citation for published version (Harvard):
Singh, NS, Stafford, J & Gao, N 2023, 'Dropwise and liquid-jet laminar flow of subcooled water falling over horizontal tube banks', *International Journal of Heat and Mass Transfer*, vol. 206, 123936. https://doi.org/10.1016/j.ijheatmasstransfer.2023.123936

International Journal of Heat and Mass Transfer 206 (2023) 123936

Contents lists available at ScienceDirect

International Journal of Heat and Mass Transfer

journal homepage: www.elsevier.com/locate/hmt

Dropwise and liquid-jet laminar flow of subcooled water falling over horizontal tube banks

Navdeep Sangeet Singh, Jason Stafford*, Nan Gao*

University of Birmingham, Birmingham, West Mid-lands B15 2TT, United Kingdom

ARTICLE INFO

Article history:
Received 25 October 2022
Revised 29 January 2023
Accepted 3 February 2023

Keywords:
Wettability
Heat transfer
Rayleigh-Plateau instability
Capillary waves
Heat exchanger

ABSTRACT

Falling-film heat exchangers are widely used to promote heat and mass transport within industrial environments. In contemporary condensers, for example, liquid films continuously form over a tube row and impact multiple tubes beneath, resulting in a rich variety of two-phase flow phenomena, including the classical Rayleigh-Plateau instability. It is widely known that altering the contact angle of the tubes influences the heat exchangers' heat and mass transfer characteristics by changing the falling films' flow behaviour (i.e. dropwise or jet). Therefore, resolving interfacial flow characteristics, such as the Rayleigh-Plateau instability, is crucial for falling film studies as this instability may change the state of the falling film from being jet flow to dropwise/jet flow or even just dropwise. To explore this aspect, three-dimensional direct numerical simulations are used in the present work to replicate the jet instability behaviour. By employing certain mesh refinement strategies demonstrated from various case studies, the interfacial flow behaviour and jet instability have been captured, showing good agreement with experimental and theoretical data previously published. This is determined from the increased jet bifurcation and a maximum error of 2.2% of the film thickness in comparison to Nusselt's result within the bulk region of the tube. In addition, the average and local heat transfer coefficients across the first tube were compared with numerical solutions to give an average error of 3.2 and 14 %. Jet instability is found to be directly related to the amplitude of the axial pressure variations which is augmented by the growth rate of the capillary wave that travels upstream. Specifically, for contact angles of 30 and 60°, the flow is in a dropwise and dropwise/jet state due to the emergence of the Rayleigh-Plateau instability. Notably, the additional satellite droplets that materialize from the unstable jet lead to an increase in the local heat transfer coefficient of the film compared to without the Rayleigh instability improvement.

1. Introduction

The occurrence of liquid films/drops plummeting over a bundle of tubes is frequently observed within many heat exchangers such as condensers, evaporators and absorbers that are heavily used in the fields of refrigeration/cryogenics, desalination, LNG (liquid natural gas) phase change, food production plants and power plants [1–4]. For example, in a horizontal tubular absorber, as the working binary liquid mixture and water-vapour enter the system , the coolant pipes siphon the latent heat away from the vapour to be liquefied. The subcooled condensate then simultaneously mixes with the operating hot liquid to dilute its concentration as it flows and falls across the heat pipes [5]. Due to the inherent variation of surface roughness across most thermal conductive materials, some areas of the pipes are left exposed, which reduces the rate of heat and mass transfer of vapour to the liquid-film i.e. the vapour's absorption rate [6].

In addition, the hydrodynamics of the film is another contributing factor as to whether it will increase or decrease the heat or mass transfer depending on the nature of its flow (i.e. sheet, jet or dropwise regimes) [7]. The ability to capture and examine the behaviour of falling films is of great interest to guide improvement in overall efficiency of heat exchangers via surface topology modification. By investigating gravity-driven flow of falling films over multiple horizontal tube banks [8], Killion *et al.* has noted that droplet nucleation sites will form as soon as the liquid beneath the first tube starts to thicken. Specifically, as liquid is continuously driven into the droplets, the hydrostatic force starts to become dominant over the surface tension and pulls the droplet orthogonally from the tube. Hereafter, the inertial force between the liquid filament and the circumference of the droplet continuously increases under gravitational acceleration. Consequently, the capillary bridge (still being attached to the droplet) begins to shrink to a point where

* Corresponding authors.
E-mail addresses: j.stafford@bham.ac.uk (J. Stafford), n.gao@bham.ac.uk (N. Gao).

https://doi.org/10.1016/j.ijheatmasstransfer.2023.123936

Nomenclature

Symbols

a	Wave velocity (m/s)
Ar	Archimedes number
C	Specific heat capacity (J/kg•K)
Co	Courant number
d	Diameter (m)
e	Internal energy (J)
g	Gravitational acceleration (m^2/s)
Ga	Galileo number
h	Heat transfer coefficient (W/m^2•K)
k	Thermal conductivity (W/m•K)
L	Length (m)
$\dot{m}$	Mass flow rate (kg/s)
Nu	Nusselt number
P	Pressure (Pa)
Pr	Prandtl number
q_o''	Heat flux (W/m^2)
r	Radial coordinate within film (m)
R	Radius (m)
Re	Reynolds number
s	Spacing (m)
T	Temperature (K)
Δt	Timestep (s)
u	Velocity (m/s)
V	Volume (m^3)
We	Weber number
Δx	Cell size (m)

Greek Symbols

α	Volume fraction
Γ	Specific mass flow rate (kg/m•s)
γ	Surface tension (N/m)
δ	Film thickness (m)
θ	Tube angle (°)
κ	Specific heat ratio
λ	Wavelength (m)
μ	Dynamic viscosity (Pa·s)
ν	Kinematic viscosity (m^2/s)
ρ	Density (kg/m^3)

Subscripts and superscripts

b	Bulk
c	Capillary
cal	Calculated
ch	Characteristic
f	Film
g	Gas phase
in	Inlet
j	Jet
l	Liquid phase
lg	Liquid-gas phase
p	Isobaric
sg	Solid-gas phase
sim	Simulated
sl	Solid-liquid phase
t	Tube
tot	Total
v	Isochoric
w	Wall
Y	Equilibrium contact angle
y	Coordinate axis parallel to flow direction
z	Coordinate axis within the axial direction
*	Dimensionless

its surface tension overcomes the viscous force causing the bridge to collapse [8].

It should be noted that the difference in overall interfacial tension force between the tip and the bulk of the jet forces the jet to retreat towards the tube [9,10]. This is then followed by a capillary wave (formulated at the tip) that propagates along the liquid jet. When the wavelength surpasses the circumference of the jet, the surface area of the filaments will decrease resulting in a reduction in surface energy. The diminished surface energy is then converted into kinetic energy which dissipates along the stream causing the jet to be perturbated [10,11]. These oscillations directly affect the Laplace pressure gradient within the fluid, forming regions of high and low pressures along the convex and concave curvatures [12]. As a result, along the high-pressure regions, the jet bifurcates into many satellite droplets [12]. Droplets that formulate from a perturbated liquid column are associated with the Rayleigh-Plateau instability [13–15].

In order to apprehend and understand such comprehensive physics within the Rayleigh time-scale [16], numerical simulations are required to locally analyse the hydrodynamic flow pattern to distinguish which properties or parameters will globally affect the proficiency of heat and mass exchangers. Further, interpreting the Rayleigh-Plateau instability is of the utmost importance to encapsulate within numerical simulations as the capillary ripples generated on the film will induce film waviness. The increased waviness of the film will provoke hydrodynamic instabilities which can increase the departure rates of droplets beneath the tube. Furthermore, such physical interaction will cause the interfacial area to increase as the additional capillary waves generated will stretch the liquid film further [8]. This will enhance the overall heat transfer as the thermal resistance between the bulk liquid and solid is reduced with the reduction in film thickness. To capture this phenomenon numerically, high-level mesh refinement is required within the liquid filament to resolve the capillary waves during the evolution of the Rayleigh-Plateau instability.

A study by Deshpande *et al.* focused on a mesh independence analysis on the retraction of a laminar liquid column by altering the number of grid points across the diameter of the jet [17]. Within the initial stages of instability, it was found that the mesh resolution was independent upon the retraction velocity and jet contour. However, as the amplitude of the capillary wave started to increase, the larger number of grid points per diameter (between 8 and 32) showed greater rapid bulging of the liquid column and jet bifurcation. At a grid resolution of 32 points within a particular timeframe, droplet pinching was observed although lower grid resolutions did not apprehend this. It should be noted that during jet instability, the diameter at the convex regions of the jet will decrease to its smallest mesh size. Therefore, the neck diameter at that particular region is limited to the number of grid points acting along its interface as it is directly proportional to the interfacial tension force [17]. Ultimately, the required number of grid points varies, depending on the film Reynolds and Weber numbers. In the context of falling films, the Reynolds number, Re_f, is given as follows [18]:

$$Re_f = \frac{4\Gamma_{in}}{\mu_l} \tag{1}$$

where μ_l is the dynamic viscosity and Γ_{in} is the inlet specific film flow rate (kg/m•s), given by the following equation,

$$\Gamma_{in} = \frac{\dot{m}_{in}}{2L_t} \tag{2}$$

where L_t is the tube length (m) and $\dot{m}_{in}$ is the mass flow rate at the inlet (kg/s). The Weber number represents the ratio of the in-

ertial to surface tension forces:

$$We_l = \frac{\rho_l (u_{l,y})^2 \lambda_c}{\gamma_{lg}} \tag{3}$$

Here, ρ_l is the density of liquid film (kg/m^3), $u_{l,y}$ is the film velocity perpendicular to the direction of tubes (m/s) and λ_c is the capillary length of the fluid of interest (m). Shinjo *et al.* stated that the mesh spacing should typically be at least a fifth of the jets' diameter to capture the profile of instability [19]. Nevertheless, as the film Reynolds number increases (i.e. the inlet velocity) the Weber number will simultaneously increase as it is proportional to the film velocity. In turn, this will increase the instability of the liquid jet and reduce the diameter of the subsequent satellite droplets following from Rayleigh-Plateau instability. As a consequence, further mesh refinement is needed to capture these droplets which may require a few hundred million grid points for a singular liquid jet. On the other hand, to find out whether numerical results are correctly captured with the selected grid spacing requires the inspection of the waviness of the jet in which the formation of oscillating droplets can be identified. This will indicate how precise the interfacial surface tension has been captured [19].

Many have attempted to model and compare the kinematics of falling films in comparison to experimentally obtained results. Hosseinnia *et al.* numerically investigated how the falling-film flow regime affects the absorption rate of water vapour within a lithium bromide (LiBr) solution whilst traveling over cooled heat pipes [20]. However, the Rayleigh-Plateau instability seen on the liquid-jet was only slightly captured, that is, only a few subsequent liquid droplets were broken from the jet after droplet detachment. As mentioned previously, this will ultimately affect the flow regime beneath the second pipe and hence the water vapour absorption rate. Ding *et al.* also compared numerical simulations against the experiments from Killion *et al.*, and extended their investigations to explore the effect of surface wettability on the hydrodynamics [18]. Nevertheless, as the Rayleigh-Plateau instability was underresolved, it remains unclear how the true flow regime on the second tube (and so on) will be as a function of surface wettability.

As briefly mentioned, changing the surface wettability of tube walls can significantly improve the heat transfer characteristics of heat exchanger systems. However, the wettability requirements for each type of system (for example, absorbers and condensers) are distinctive. Firstly, when a liquid droplet is in kinetic equilibrium on an ideally flat solid surface, three governing surface tension forces co-exist [21]. Their direction and magnitude will affect the droplet's equilibrium contact angle from which surface wettability is determined. This relationship is commonly expressed as the Young's equation:

$$\cos\theta_Y = \frac{\gamma_{sg} - \gamma_{sl}}{\gamma_{lg}} \tag{4}$$

where θ_Y is known as the equilibrium (or intrinsic) contact angle (°), γ_{sg} is the solid-gas interfacial tension (N/m), γ_{sl} is the solid-liquid interfacial tension and γ_{lg} is the liquid-gas interfacial tension. Furthermore, a number of widely known wetting thresholds are prescribed from the extent of the contact angles. For example, a superhydrophobic surface signifies that a water droplet has a contact angle more than or equal to 150° [22]. In relation, a hydrophobic surface is when the droplet displays a contact angle more than or equal to 90° [22]. These two states indicate that a surface can be non-wettable or partially wettable. Conversely, a hydrophilic surface promotes a contact angle of less than 90°. Further decreasing this state leads to a fully wetted substrate known as a superhydrophilic surface where the contact angle is less than 10° [22]. In a partial wetting regime, droplets that are associated with a microscopic thin film absorbed within their vicinity will have reduced tendency to move laterally and longitudinally [23].

To elaborate on different heat exchanger wettability requirements, an absorber heat exchanger (or an evaporator) will favour a completely wetted surface (as momentarily stated beforehand). This is reflected from the previous work by Köroglu *et al.*, who fabricated functional hydrophilic and hydrophobic surfaces upon copper heat pipe banks to investigate the heat transfer enhancement on a falling-film evaporator [24]. It was noted that the functional hydrophilic surface exhibited better performance in comparison to the plain and hydrophobic surface. This was due to the increased affinity of the surfaces to water, promoting a thin liquid film along the interface. In respect to absorbers, the hydrophilic surface property increased the diffusion rate of the vapour onto the surface, which explains the improvement in the heat transfer rate. Subsequently, Zheng *et al.* studied the same effect on a falling-film evaporator but further modified the surface to reach a superhydrophilic condition [6]. As anticipated, the heat transfer coefficient of the superhydrophilic surfaces outperformed the hydrophilic surface by at least twice the amount at low film flow rates due to complete surface wetting at low spray densities.

During steam condensation within a condenser, when the supersaturated vapour falls onto bare subcooled heat pipes, the natural hydrophilic quality of the material promotes filmwise condensation. This mode of condensation presents itself as a thin liquid film across the surfaces, which induces additional thermal resistance between the vapour and the cooled surface. To repel the liquid film, a hydrophobic or superhydrophobic surface is needed which can induce dropwise or even jumping-droplet condensation [25]. Recently, Zhang *et al.* fabricated superhydrophobic and hydrophobic surfaces upon copper heat pipes which were then placed in a condenser to assess their heat transfer performance [26]. At low subcooling temperatures (less than 12 K) the hydrophobic surfaces outperformed the original surface in terms of heat transfer coefficient and heat flux, whilst the superhydrophobic surface exponentially enhanced the heat transfer rates. This was due to dropwise and jumping-droplet condensation being established on the hydrophobic and superhydrophobic surfaces. These modes of condensation enabled the exposure of the working surfaces, which promptly reduced the thermal resistance between the vapour and solid interface.

In this study, we present direct numerical simulations designed to resolve the Rayleigh-Plateau instability and other interfacial flow features of the falling film within the dropwise regime by focusing on mesh refinement within the liquid-jet. The flow phenomena on the first and second tubes is directly compared to the experimental results by Killion *et al.* [8]. In addition, the local heat transfer coefficient within the film is assessed to explore the effects of additional satellite droplets impacting the tube. Moreover, effects of static contact angles are parametrically investigated across a wide range of surface conditions from superhydrophilic to superhydrophobic states. The distinction between the wettability states is quantified from the hydrodynamics of the flow pattern (i.e. capillary wave propagation), changes in droplet departure diameter, film waviness and instability, transition periods from dropwise to jet flow and the film thickness across the impacted tubes.

2. Methodology

2.1. Geometry setup, boundary conditions and mesh refinement

Firstly, to validate the numerical predictions, a similar tube configuration as the experiments of Killion *et al.* was generated [8]. The system consisted of six horizontal brass tubes in a 300-mm long column. The outer tube diameter (d_t) and the longitudinal tube spacing (s_t) (distance between the tube faces) was 12.7 mm and 25.4 mm (double the tube diameter). To feed the water over the tubes, a distributer was placed 1 mm above the first tube. This

was to ensure that the fluid impacting the tube would be evenly distributed i.e. verifying that the planar shear stresses at the walls would be negligible so that certain parabolic velocity profiles may not be created and disturb the flow.

To reduce computational power and time, only three horizontal tubes are selected for the simulation model where their length is equivalent to the Rayleigh-Taylor instability wavelength. The Taylor wavelength is known as the distance between the droplets on the pipe where they start to nucleate from and leave. This was first noted by Hu *et al.* [7] who observed this behaviour and discussed the accuracy of the different correlations of other researchers used to determine the Taylor wavelength on horizontal tubes. However, as suggested by Ding *et al.* [18], most studies ignored the effects of the film Reynolds and Galileo numbers on the Taylor instability. Nevertheless, Armbruster *et al.* took this into consideration and correlated the Taylor wavelength equation with a standard deviation of ±7.5% as [27]:

$$\lambda = \frac{2\pi\sqrt{2}}{\sqrt{\frac{\rho_l g}{\gamma_{lg}}\left(1+\left(\frac{\frac{Re_f}{2}}{Ga^{\frac{1}{4}}}\right)^{0.8}\right)+\frac{2}{d_t^2}}} \tag{5}$$

where g is the gravitational acceleration (m^2/s), and Ga is known as the Galileo number. The Galileo number is widely known as the ratio of gravitational (i.e. buoyancy) to viscous forces of a liquid. The general Galileo number is given as:

$$Ga = \frac{g\lambda_c^3\rho_l^2}{\mu_l^2} \tag{6}$$

For falling films, the length scale, λ_c, is commonly expressed as the capillary length which is known as:

$$\lambda_c = \sqrt{\frac{\gamma_{lg}}{\rho_l g}} \tag{7}$$

By squaring the Galileo number and inserting the capillary length, one gets a modified Galileo number, Ga^*, shown below [7],

$$Ga^* = \frac{\rho_l\gamma_{lg}^3}{\mu_l^4 g} \tag{8}$$

To ensure that dropwise flow is initially maintained from the tube banks, the film Reynolds number must be within a certain threshold. According to Hu *et al.*, the regime for which dropwise flow will occur is [7]:

$$Re_f = 0.074Ga^{*0.302} \tag{9}$$

with a mean deviation of ±11% [7]. In addition, the transition regime of which dropwise flow will evolve into jet flow (i.e. dropwise/jet flow) is verified as:

$$Re_f = 0.096Ga^{*0.301} \tag{10}$$

having a mean deviation of ± 11.2% [7]. For water at approximately room temperature and at atmospheric pressure, the critical Reynolds number where dropwise flow is maintained is given as Re_f = 116 from Eq. (9). Based on this, the critical inlet specific film-flow rate from Eq. (1) is Γ_{in}= 0.029 kg/m•s. It should be noted that the Reynolds number must be kept less than 100 as this is typically the Reynolds number margin observed from the experiments by Killion *et al.* to establish droplet-to-droplet/jet behaviour [8]. To make a direct comparison against the simulation results by Ding *et al.*, a Reynolds number of Re_f = 80 was selected which corresponded to an inlet specific film-flow rate of Γ_{in} = 0.02 kg/m•s. The tube length was chosen as 22 mm (rounded up from 21.7 mm) for these flow conditions based on the Taylor wavelength (Eq. (5)). The dimensions of the inlet feeder were fixed at 1×2 mm^2 (L_z x L_x) and positioned 1 mm above the first tube. This arrangement limits the effects of shear forces created from the feeder which could perturb the liquid flow around the tube and invalidate the results [18,20]. The length of the domain in the flow direction was also chosen to match that of the numerical study by Ding *et al.* [18] which corresponds to 99.9 mm.

To further note, in order to predict and validate the heat transfer model prescribed, the Nusselt number can be used to describe the heat and mass transfer characteristics for each of the falling film regimes. The Nusselt number is widely known as the ratio of the convective to the conductive heat transfer rate of a fluid, which is normally expressed as:

$$Nu = \frac{h\lambda_c}{k_l} \tag{11}$$

where h is the convective heat transfer coefficient (W/m^2•K) and k_l the thermal conductivity of the liquid (W/m•K). For falling films, the length scale here is denoted based on the characteristic film thickness (δ_{ch}), which is given as [7,28]:

$$\delta_{ch} = \sqrt[3]{\frac{\nu_l^2}{g}} \tag{12}$$

with ν_l being the kinematic viscosity of the liquid (m^2/s). Therefore, substituting δ_{ch} for λ_c one obtains a modified Nusselt number, Nu^*,

$$Nu^* = \frac{h}{k_l}\sqrt[3]{\frac{\nu_l^2}{g}} \tag{13}$$

From the experimental observations made by Hu *et al.*, the resulting Nusselt number correlation established for dropwise flow is expressed as [7]:

$$Nu^* = 0.113Re_f^{0.85}Pr^{0.85}Ar^{-0.27}\left(\frac{s_t}{d_t}\right)^{0.04} \tag{14}$$

with a mean deviation of ± 6.1% [7]. Here, Pr is known as the Prandtl number and Ar is given as the Archimedes number. The Prandtl number illustrates the ratio of the momentum diffusion rate to the thermal diffusion rate of the fluid which is given as:

$$Pr = \frac{\mu_l c_{p,l}}{k_l} \tag{15}$$

Likewise to the Galileo number, the Archimedes number represents the ratio of the gravitational to the viscous forces of a fluid but instead as a function of the tube diameter [7]. Therefore, the length scale in this case is equivalent to the tube diameter ($\lambda_c = d_t$), and one finds the Archimedes number as,

$$Ar = \frac{\rho_l^2 g d^3}{\mu_l^2} \tag{16}$$

Also, the dimensionless parameters stated within the Nusselt correlation equations were spanned in this work to a certain range for which Hu *et al.* experiments were conducted up to, with Re_f = 4 – 2060, Pr = 4.8 – 75.6, Ar = 6.7 × 10^5 – 1.8 × 10^8 and the ratio between the tube spacing and diameter, $(\frac{s_t}{d_t})$ = 0.3 – 5.2 [7].

Constant thermodynamic and fluid properties for water and air were implemented which are evaluated at the inlet temperature (T_{in} = 20°C), where ρ_l = 998.2 kg/m^3, μ_l = 1.003 × 10^{-3} Pa•s, $C_{p,l}$ = 4182 J/kg•K, k_l = 0.6 W/m•K, ρ_g = 1.225 kg/m^3, μ_g = 1.79 × 10^{-5} Pa•s, $C_{p,g}$ = 1006.43 J/kg•K, k_g = 0.02587 W/m•K and γ_{lg} = 0.072 N/m. A symmetric boundary condition was imposed which permitted simulations of the complex two-phase flows while also reducing the computational domain size and resource demands. As shown in Fig. 1a, a velocity-inlet is prescribed at the 1×1 mm^2 sectioned area with a secondary velocity-inlet

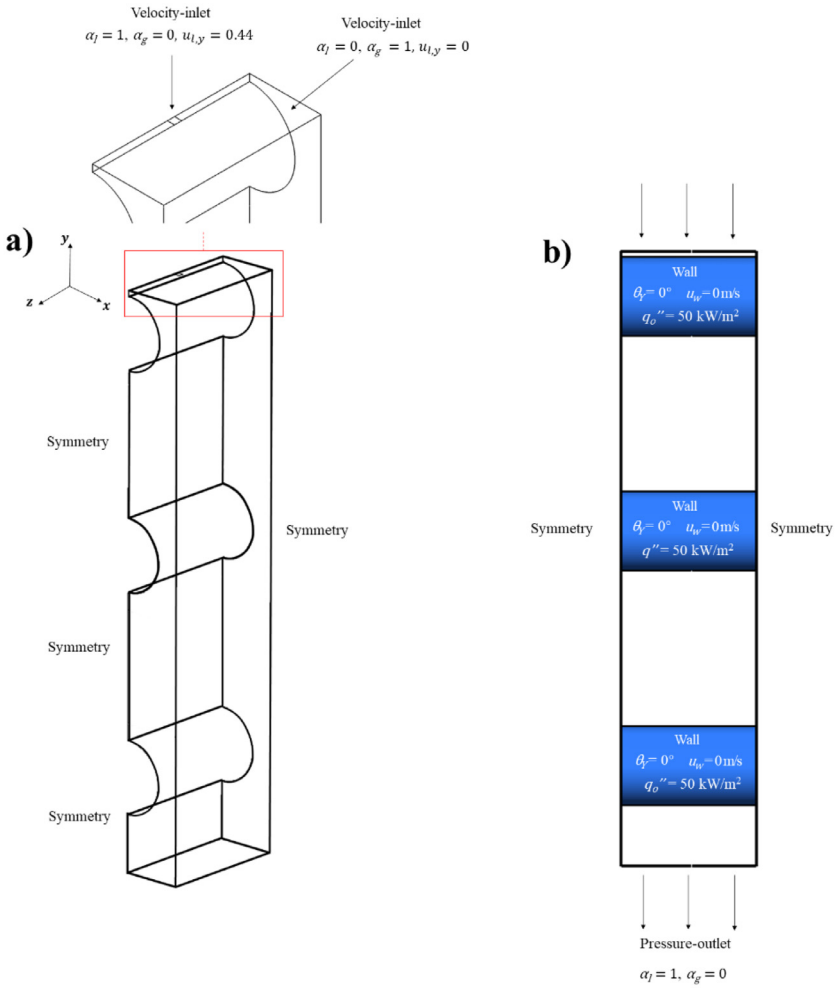

Fig. 1. (a-b) Computational fluid domain with defined boundary conditions.

opted around the domain of the feeder. A liquid volume fraction of 1 (α_l) is imposed at the inlet feeder to ensure only water-liquid enters the domain from that area whilst a gas volume fraction (α_G) of 1 is selected for the secondary velocity inlet as this particular region will represent the atmosphere. A constant velocity of $u_{l,y} = 0.44$ m/s was imposed at the feeder which was calculated from Eq. (2) using the operating Reynolds number ($Re_f = 80$). At the minor inlet, $u_y = 0$ m/s since no external airflow is present there. Symmetry boundary conditions are applied at the lateral cross-section of the tubes and at the front, back and side faces of the domain to reduce the number of mesh elements required by duplicating the current geometry normal to these directions.

It should be nonetheless noted, for large contact angles ($\geq 90°$), the symmetry boundary conditions on the left-hand side of Fig. 1a must be changed to pressure-outlet as some formulating droplets on the tubes escape the fluid domain. From Fig. 1b a pressure-outlet is enforced at the bottom of the domain having a gauge (or static) pressure of 0 Pa since the environment surrounding the tubes is only exposed to atmospheric pressure (101325 Pa). An intrinsic contact angle of 0° ($\theta_Y = 0°$) was initially subjected on each of the three tube walls, which will create a more accurate representation of the fluid flow near the top section of the tubes. As the effect of contact angle hysteresis is not included in this study, the contact angle hysteresis is assumed to be 0°, where the advancing and receding contact angles are equal to the equilibrium contact angle. Subsequently, a no-slip condition ($u_w = 0$ m/s) was also applied at the walls, whereas the finite slip velocity practically experienced by the fluid at the solid-liquid interface is considered to be negligible for the characteristic length scale. Finally, a uniform heat flux, q_o'', supplied to the tube walls was equal to 50 kW/m^2 based on the experimental parameter range by Hu *et al.* [7].

The fluid domain had been meshed using hexahedral elements as shown in Fig. 2. According to mesh sensitivity analyses conducted by Ding *et al.* and Hosseinnia *et al.*, respectively, the global mesh size was selected to be 0.25 mm with the local mesh size being 0.2 mm around the face of the tube walls [18,20]. To sufficiently capture the hydrodynamic and thermal boundary layers around the tube walls, additional refinement layers were added as seen in Fig. 2a. Sixteen grid points per unit jet length were used to capture the fine-scale interfacial flow features of the jet, equivalent to a cell length of 0.1 mm displayed in Fig. 2b-c (based on the smallest jet length observed that was 1.6 mm) [17]. Increasing grid resolution to 24 and 32 grid points resulted in limited improvements in resolving the jet instability and droplet breakup. The concluded cell length was then used to locally refine the mesh near the jet at the front and lateral planar faces.

2.2. Governing equations and numerical schemes

To track the liquid-gas interface of an incompressible, Newtonian, laminar fluid, the Volume of Fluid (VOF) method was used to determine the volume fraction of the individual phases:

$$\frac{1}{\rho_q}\left(\frac{\partial}{\partial t}(\alpha_q \rho_q) + \nabla \cdot \left(\alpha_q \rho_q \vec{v_q}\right)\right) = 0 \tag{17}$$

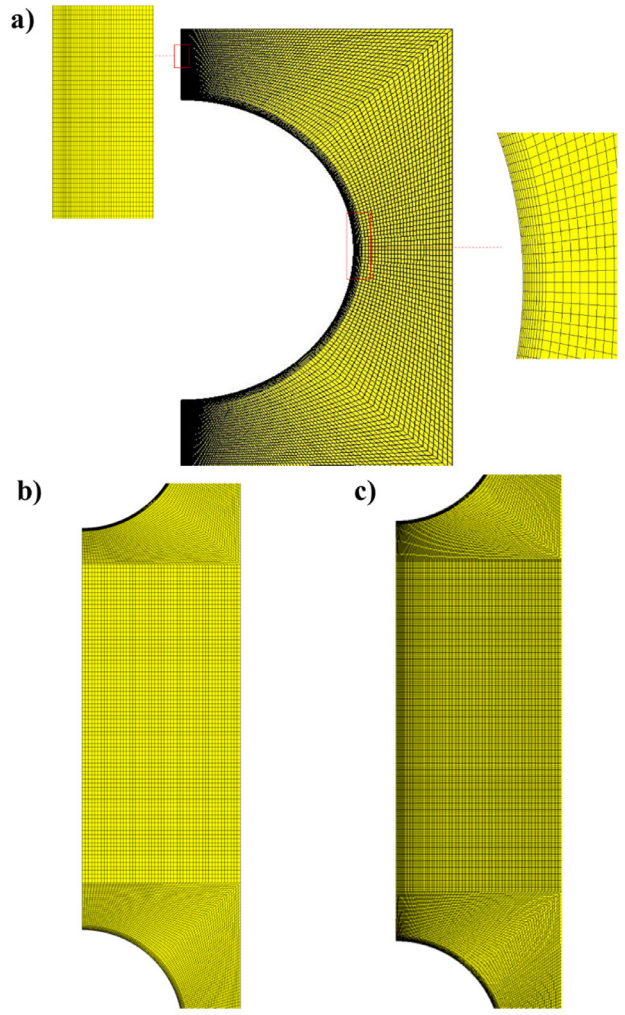

Fig. 2. (a) Mesh refinement near the tube walls with additional inflation layers added at tube wall interface to capture the liquids' film thickness and hydro/thermodynamic flow displayed on the front plane of the second tube. (b) Planar view of mesh topology at the middle section between the first and second tubes without mesh refinement (0.25 mm), (c) with mesh refinement (0.1 mm).

where q stands for the liquid phase (l) or gas phase (g). The velocity field in the fluid domain is predicted using the momentum equation:

$$\frac{\partial}{\partial t}(\rho\vec{v}) + \nabla\cdot(\rho\vec{v}\vec{v}) = -\nabla p + \nabla\cdot\left[\mu\left(\nabla\vec{v} + \nabla\vec{v}^{T}\right)\right] + \rho\vec{g} + \overrightarrow{F_{vol}} \tag{18}$$

As the velocity field is divided across the phases involved (i.e. solved within the mixture phase where a cell contains a value $0 < \alpha_q < 1$), the density and viscosity values in the transport equation are computed according to:

$$\rho = \alpha_l\rho_l + (1-\alpha_l)\rho_g \tag{19}$$

$$\mu = \alpha_l\mu_l + (1-\alpha_l)\mu_g \tag{20}$$

where $(1-\alpha_l) = \alpha_g$ since the volume fraction equation is solved only using the secondary phase (α_l).

$\overrightarrow{F_{vol}}$ is given as a source term which is used to interpret the surface tension force upon the liquid interface. The continuum surface tension force (CSF) model developed by Brackbill *et al.* [29] is used to establish the interfacial force by calculating the pressure gradient along the interface. If only two phases are present, then this is represented as:

$$\vec{F_{vol}} = \gamma_{lg}\frac{\rho K\nabla\alpha_l}{\frac{1}{2}(\rho_g+\rho_l)} \tag{21}$$

The temperature field defined in the fluid domain is derived from solving the energy equation in the mixture phase:

$$\frac{\partial(\rho e_t)}{\partial t} + \nabla\cdot[\vec{v}(\rho e_{tot}+p)] = \nabla\cdot[k\nabla T] \tag{22}$$

Here, e_{tot} is given as the total internal energy $\left(e_{tot} = e + \frac{v^2}{2}\right)$, where e is the internal energy defined as $e = c_v(T)$, with c_v being the isochoric specific heat capacity (J/m^2•K) and T the temperature (K). p is the pressure based on the ideal gas law ($p = (\kappa-1)\rho e$) where κ is equal to specific heat ratio ($\kappa = \frac{C_p}{C_v}$). The thermal conductivity, k, is calculated in the mixture phase as:

$$k = \alpha_l k_l + (1-\alpha_l)k_g \tag{23}$$

The local surface curvature of the liquid-gas interface, K, is defined as the divergence of the unit normal vector given as [29]:

$$K = \nabla\cdot\hat{n} \tag{24}$$

where $\hat{n}$ is specified from the volume fraction gradient of the liquid phase.

$$\hat{n} = \frac{\nabla\alpha_l}{|\nabla\alpha_l|} \tag{25}$$

Similar to the theory proposed by the CSF model, the surface adhesion force associated to the magnitude of the contact angle (θ_Y) imposed at the wall is computed using the wall adhesion model. By selecting a contact angle value, the unit normal vector adjacent to the wall is adjusted as:

$$\hat{n} = \hat{n}_w\cos\theta_Y + \hat{t}_w\sin\theta_Y \tag{26}$$

where $\hat{n}_w$ and $\hat{t}_w$ are the unit vectors that are normal to and tangent from the wall. The volume fraction and momentum equations are solved using an explicit discretisation scheme to reduce the complexity of solving the equations. As a consequence, this reduces the robustness of the simulation stability and requires small time-steps to counteract this problem. In terms of numerical stability, to sufficiently capture the capillary wave propagation rate along the jet without divergence, the simulation must record the fluid dynamics within a unit cell as the capillary waves propagate through each cell. To achieve this, an adaptive time-stepping method was required to adjust the timestep in accordance with the wave velocity (e.g. the faster the waves propagate, the smaller the timestep must be). This relationship can be expressed as Courant–Friedrichs–Lewy condition otherwise known as the Courant number [30].

$$Co = \frac{a\Delta t}{\Delta x} \tag{27}$$

Here, a is given as wave velocity (m/s), Δt is the timestep (s) and Δx is the distance between the elements (m). When the Courant number is greater than one, numerical instability will start to arise as fluid particles begin to navigate through two or more elements at a given timestep. This causes the numerical diffusion (or the viscous diffusion coefficient) to become negative which makes the solution to the governing equations multiply indeterminately. To avoid this, a maximum Courant number of 0.4 was set. The global timestep was automatically adjusted during the simulation to meet this requirement.

In order to ascertain the average heat transfer coefficient across the tube, the local heat transfer coefficient must first be solved. Notably, the heat transfer coefficient will vary across the circumferential and axial direction (θ, z) as the liquid spreads. Based on

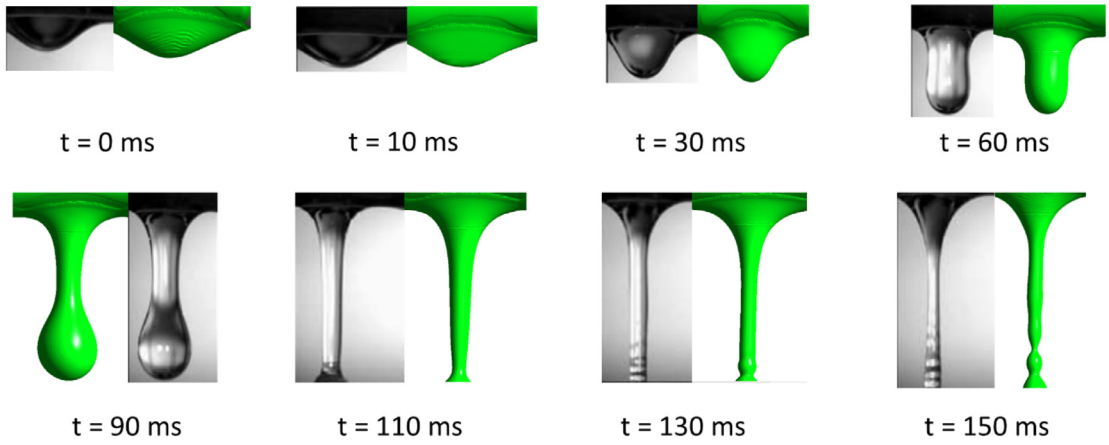

Fig. 3. Evolution of droplet formation and Rayleigh-Plateau instability along the liquid bridge that is established during droplet detachment from the first tube. Compared against Killion et al. experimental results [8].

Newton's law of cooling, the local heat transfer coefficient is given as:

$$h(\theta, z) = \frac{q_o''}{T_w(\theta, z) - T_{in}} \tag{28}$$

where T_w is the wall temperature (K). Thus, the average heat transfer coefficient, $\bar{h}$, is computed by doubly integrating the local heat transfer coefficient on the surface area of the tube assuming the entirety of the surface provides a uniform heat flux:

$$\bar{h} = \frac{1}{2\pi R_t L_t} \iint h(\theta, z)\, dA \tag{29}$$

Here R_t is the radius of the outer tube surface (m). By calculating the average heat transfer coefficient, the average Nusselt number, $\overline{Nu}$, of the tube surface is obtained by substituting $\bar{h}$ into h from the modified Nusselt Eq. (13).

$$\overline{Nu} = \frac{\bar{h}}{k_l} \sqrt[3]{\frac{v_l^2}{g}} \tag{30}$$

Furthermore, the coupling of the pressure and velocity correction gradients in the simulation were solved using the PISO (Pressure-Implicit with Splitting of Operators) algorithm. The PISO method is suitable for transient cases as the pressure and velocity gradient calculations are repeated indefinitely until the continuity and momentum equations are satisfied. This is signified from having a normalized residual mean square value of $\leq 10^{-5}$ [18]. In addition, the mass, momentum and energy equations were spatially discretised using the PRESTO (PREssure STaggering Option) and the second-order upwind scheme. Correspondingly, the Geo-Reconstruct scheme is used to interpolate the advection between the liquid and gas interface by assuming a piecewise-linear slope [31]. Finally, the transient scheme used to solve the unsteady-state differential in the mass and momentum equations was first-order upwind, as high order schemes are restricted to implicit solvers in ANSYS Fluent.

3. Results and discussion

3.1. Numerical validation

Figure 3 illustrates the droplet detachment process assessed at different timesteps and evaluated against experimental results by Killion *et al.* [8]. The simulation results show good agreement with the hydrodynamics observed in the necking progression of the pendent droplet. After the droplet detaches itself from the liquid bridge (at 130 ms), the break-up of the liquid filament is initiated by the harmonic oscillations generated from the jet recoil. The simulations adequately capture this phenomenon due to the mesh refinement around the liquid-jet, while also capturing the axial motion of the droplet during droplet nucleation (from 0 to 10 ms). A pendent droplet that nucleates on a horizontal tube tends to elongate towards the axial direction due to the competing surface tension and gravitational forces [8]. However, once the gravitational force overcomes the surface tension force, the pendulous droplet departs away from the tube. Due to its initial axial translation, the shape of the droplets appears to be asymmetrical (seen from 90 ms onwards).

To quantitatively validate the hydrodynamics of the falling film around the first tube, the Nusselt solution can be used to verify the expected film thickness and velocity profile within a two-dimensional plane. The Nusselt's film thickness for falling films upon a tube can be expressed as [32]:

$$\delta = \left(\frac{3\mu_l \Gamma_{in}}{\rho_l^2 g \cos\theta} \right)^{\frac{1}{3}} \tag{31}$$

where θ is the circumferential angle around the tube (°). Additionally, the circumferential and radial velocity profiles around the tube can be calculated as:

$$u_\theta = \frac{\rho_l g}{\mu_l} \sin\theta \left(\delta r - \frac{r^2}{2} \right) \tag{32}$$

$$u_r = -\frac{\rho_l g}{R_t \mu_l} \cos\theta \left(\frac{\delta r^2}{2} - \frac{r^3}{6} \right) - \frac{\rho_l g}{2R_t \mu_l} r^2 \sin\theta \frac{d\delta}{d\theta} \tag{33}$$

where r is the radial coordinate within the film (m). From Fig. 4, the three-dimensional numerical film thickness located at the mid-plane (11 mm) is displayed when t = 2 s and plotted against the two-dimensional Nusselt's film thickness. As shown, the numerical film thickness is validated against the Nusselt's solution with a maximum error of 2.2% between 7 and 129° (clockwise). However, exceptions are made at the top of the tube and towards the bottom of the tube. The enlarged necking seen at the top of the tube is attributed to the surface tension effect of the inlet feeder. And the droplet formation (seen roughly 38° from the tube counter-clockwise) is due to the symmetry boundary condition enforced which creates a contact angle of 90° at the symmetric interface. This makes the solid-gas surface tension become equal to the solid-liquid surface tension (as seen from Eq. (4)) which allows the fluid to be seemingly in contact with air (from a real-world perspective). It should be noted that the Nusselt's solution ignores the effects of surface wettability which results in no droplet formation and only filmwise flow.

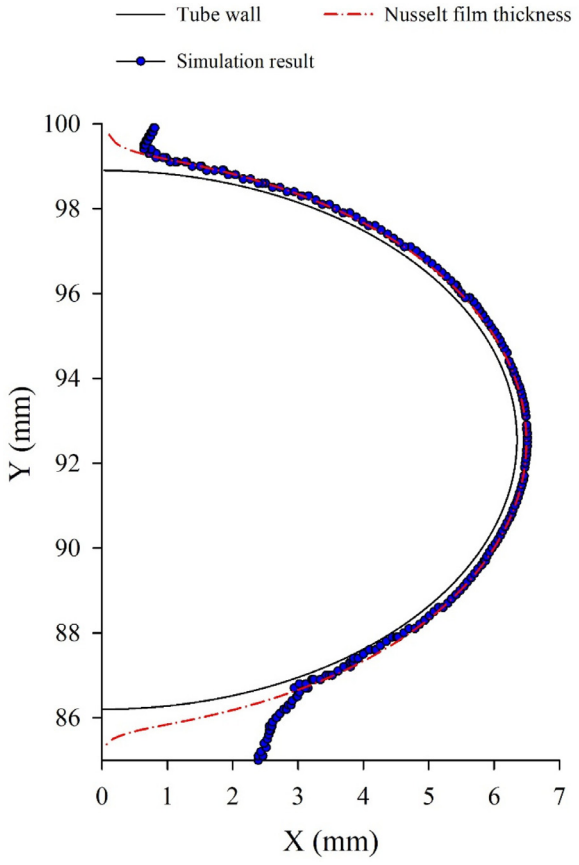

Fig. 4. Film thickness predictions against Nusselt's model. Results are extrapolated from the first tube at the mid-plane (L = 11 mm) when t = 2 s.

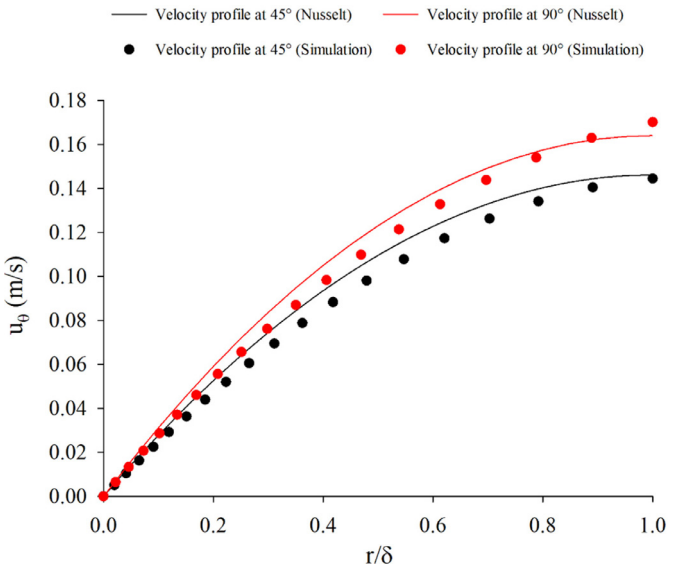

Fig. 5. Circumferential velocity profile calibration around the first tube at different circumferential angles when L = 7.3 mm at t = 2 s.

Furthermore, the circumferential velocity profiles at a tube length of 7.3 mm across the first tube is shown in Fig. 5. The velocity profiles chosen for validation were selected away from the middle of the tube due to the droplet formation, which will alter the velocity profiles presented due to the three-dimensional flow affecting the circumferential velocity around the tube as stated by Ding *et al.* [18]. Nonetheless, the simulated velocity profiles coincide with the Nusselt's velocity profiles well for circumferential angles of 45° and 90° with a maximum error of 10.6 % for 45° and 9 % for 90°. The deviation between the theoretical and simulation results is due to the effect of film waviness along the axial direction which is neglected in the Nusselt solution.

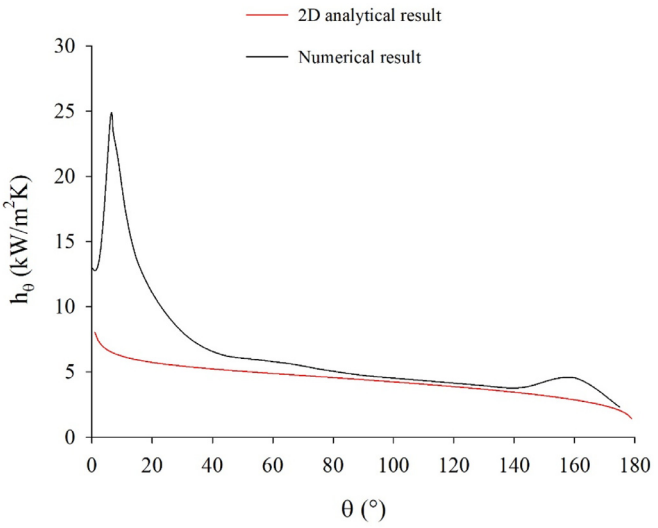

Fig. 6. Local heat transfer coefficient within the liquid film across the circumferential direction at a tube length of 11 mm when t = 2 s at the first tube compared against the heat transfer model by Rogers et al. [33].

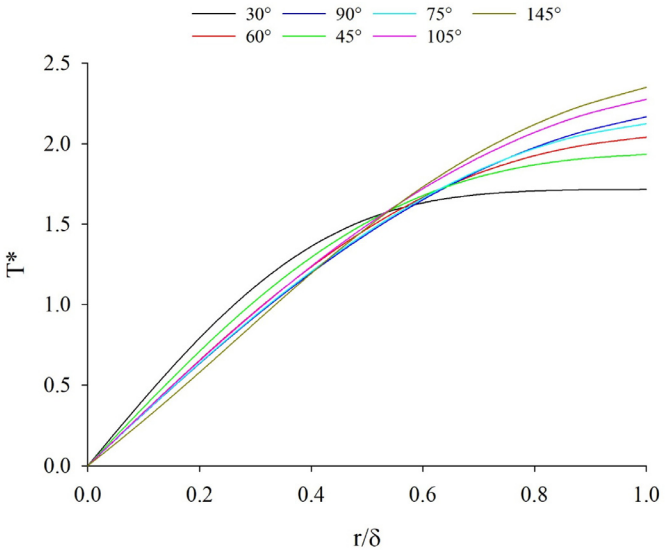

Fig. 7. Dimensionless circumferential temperature profiles within the liquid film for different circumferential angles when L = 11 mm at t = 2 s.

To validate the heat transfer model, the average Nusselt number was recorded on the first tube and then time-averaged across 2 seconds (total simulation time). The following result gave an average Nusselt number of $\overline{Nu}_{sim} = 0.26$ (rounded up to 2 decimal places), whilst the calculated result from Hu *et al.* gave a value of $\overline{Nu}_{cal} = 0.27$ [7]. This corresponded to an error of 3.2 %. Since Hu *et al.* correlated Nusselt equation with a mean deviation of 6.1 %, the error presented is satisfactory as it is confined within the boundaries of the mean deviation. Moreover, the local heat transfer coefficient of the film was also compared against a two-dimensional analytical model by Rogers *et al.* [33]. It should be noted that the experimental study by Killion *et al.* was conducted under isothermal conditions (ambient temperature) [8]. Nonetheless, with the

analytical model, a heated tube surrounded by a running liquid film is partitioned into two regions known as the developing thermal boundary layer region and the fully-developed thermal boundary layer region. The developing thermal boundary layer region is known to begin just after liquid impingement zone where the thermal boundary layer thickness continuous to grow within the viscous (or hydrodynamic) boundary layer (for fluids with a Prandtl number greater than one) [7]. When the thermal boundary layer intersects the outer liquid film, the thermal boundary layer is considered to be fully developed causing the rate of change in the local heat transfer to approach zero (i.e. thermal boundary layers expand towards the outside of the film). In this study, the local heat transfer coefficient has been determined using the relationship for thermally developing boundary layers [7,33]:

$$\frac{hd}{k_l} = 0.831 Re^{\frac{1}{9}} Ar^{\frac{2}{9}} Pr^{\frac{1}{3}} \left(\frac{\sin\theta}{P(\theta)}\right)^{\frac{1}{3}} \tag{34}$$

where $P(\theta)$ is given to be [7,33],

$$P(\theta) = \int_0^{\theta} \sqrt[3]{\sin\theta}\, d\theta \tag{35}$$

Figure 6 displays the circumferential local heat transfer coefficient within the liquid film at the middle section of the first tube which is compared against the analytical model of Rogers *et al.* [33]. The theoretical model disregards film waviness, surface tension and liquid impingement which partly explains the large variation in the results at certain tube angles [28]. Between 0 and 6°, the heat transfer coefficient rises to its peak due to the effect of liquid impingement of the inlet feeder (the stagnation zone). Notably, the stagnation zone in this case is proportional to the width and the height of the inlet feeder. After the stagnation zone, the fluid enters the impingement region (6 to 30°) where the velocity gradient reduces due to the viscous force acting against the fluid (as illustrated in Fig. 16a). This region is analogous to the wall-jet formed in classical jet impingement flows [34], extending the

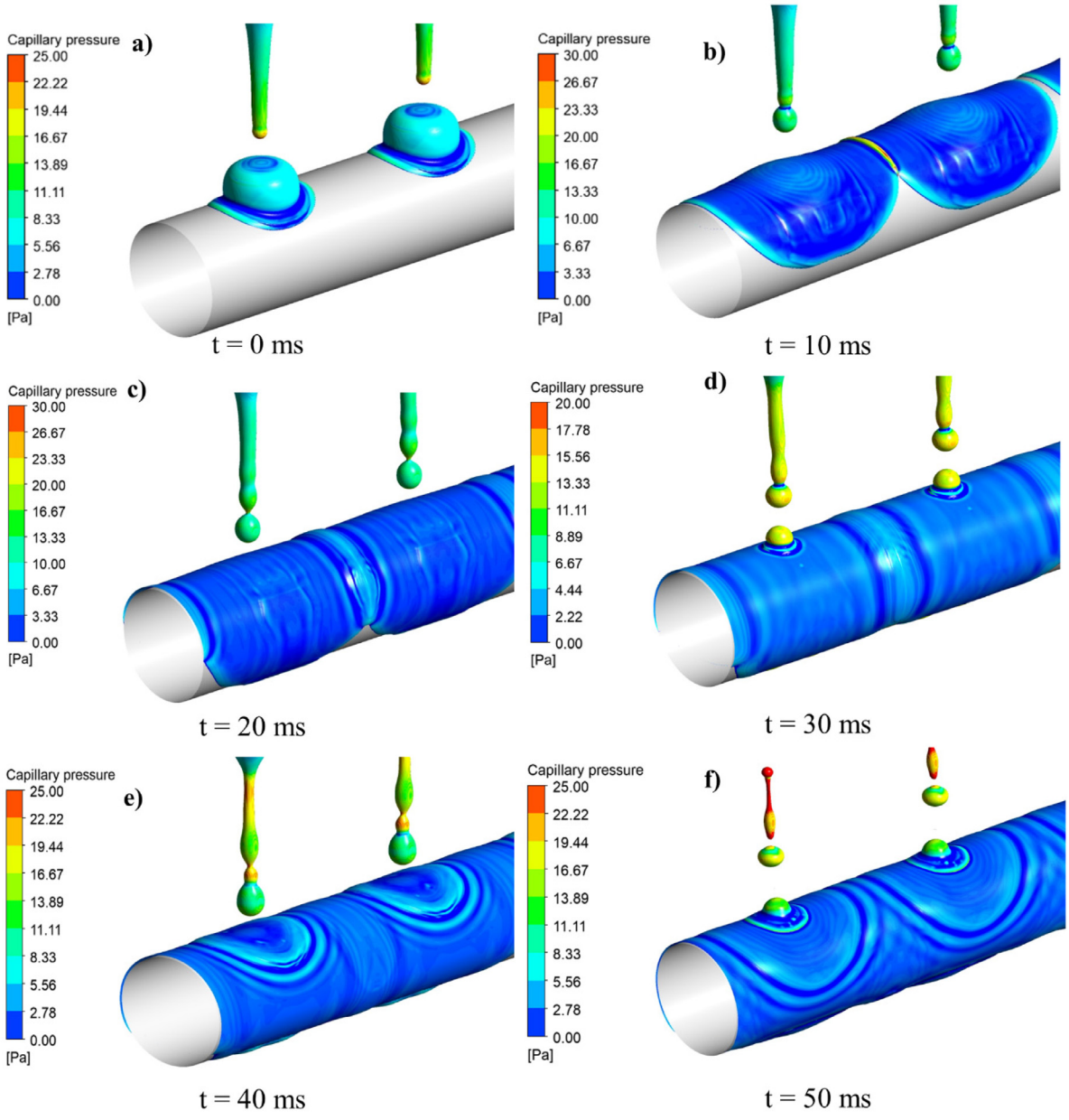

Fig. 8. Pressure contours showing capillary ripples generated from the satellite droplets and at different times after first droplet impaction upon the second tube.

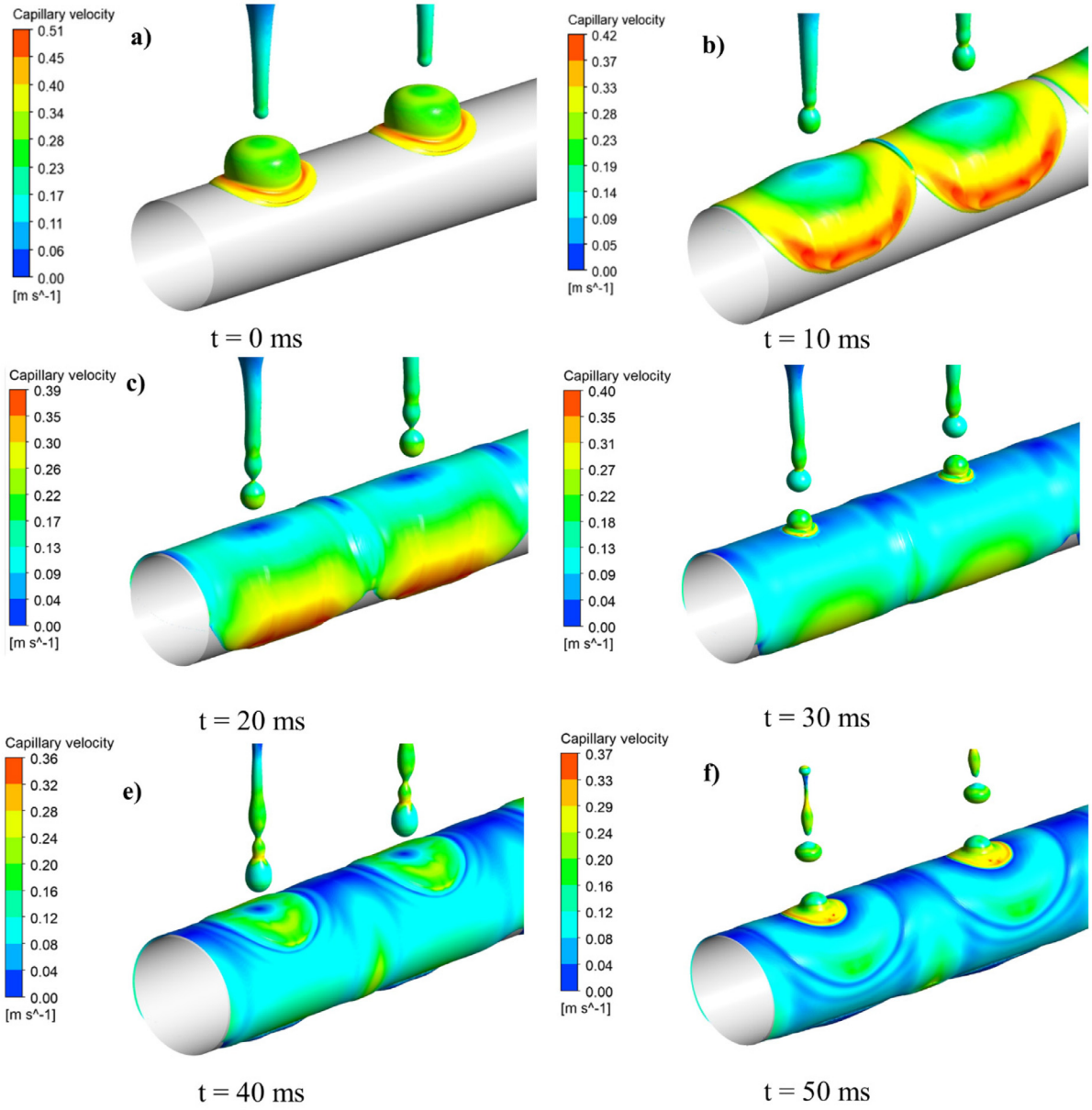

Fig. 9. Velocity contours from initial droplet impaction to Rayleigh-Plateau instability jet break-up at different timescales upon the second tube.

development region to much larger circumferential angles (~100°) and resulting in numerically simulated heat transfer coefficients that are comparable to the analytical prediction.

In this developing thermal boundary layer section, the thermal boundary thickness represented by the dimensionless temperature profile in Fig. 7 continues to increase within the liquid film. Within this region, the average difference in heat transfer coefficient is 14 % compared to Rogers *et al.* theoretical model [33]. After 145°, the thin film can no longer follow the tube contour due to flow separation and droplet formation at the end of tube. This increases the fluid velocity within the small intermediate region leading to an increase in the heat transfer coefficient from 145° to 180°. Since the analytical model disregards surface tension, this phenomenon is non-existent causing no change in the heat transfer coefficient gradient. The dimensionless temperature profile was determined as:

$$T^* = \frac{T - T_w}{T_b - T_w} \tag{36}$$

where T_b is equal to the bulk temperature of the fluid (K) which is defined as the average temperature within the liquid at a defined axis.

3.2. Implications of satellite droplet impaction on local heat transfer within a liquid film

As previously discussed, the improved capture of the jet ligament break-up will establish additional capillary ripples within the fluid which can be clearly seen in Fig. 8. At 0 ms, the droplet has successfully detached itself from the liquid filament and has started spreading more rapidly than the impact speed in the circumferential and axial directions. This is indicated from the low static pressure the fluid experiences upon impact and the negative pressure gradient between the head and the puddle of the droplets. From this, the kinetic energy of the fluids starts to increase according to Bernoulli's principle and is shown from the capillary velocity contours in Fig. 9, which was also mentioned by Killion *et al.* [8]. It should be noted, however, that this observation

is only valid for isentropic flows. After 10 ms, the droplet has now flattened into a saddle wave which then impinges onto the second saddle wave adjacent to it and formulates a liquid hoop around the tube. The hoop appears to spread circumferentially and not axially as the impact force from each of the saddle waves cancels one another, caused by the adjacent droplet impacting the tube at approximately the same time as the other. The velocity of saddle waves then starts to decline as it continuously spreads over a large portion of the tube due to the viscous forces being dominant.

From 20 ms onwards, satellite droplets start to form from the jet and impact the film which gives rise to capillary ripples generated in the circumferential and axial directions. This is also noted by Killion *et al.*, although due to lighting conditions, only axial waves could be seen [8]. The circumferential waves then travel to-

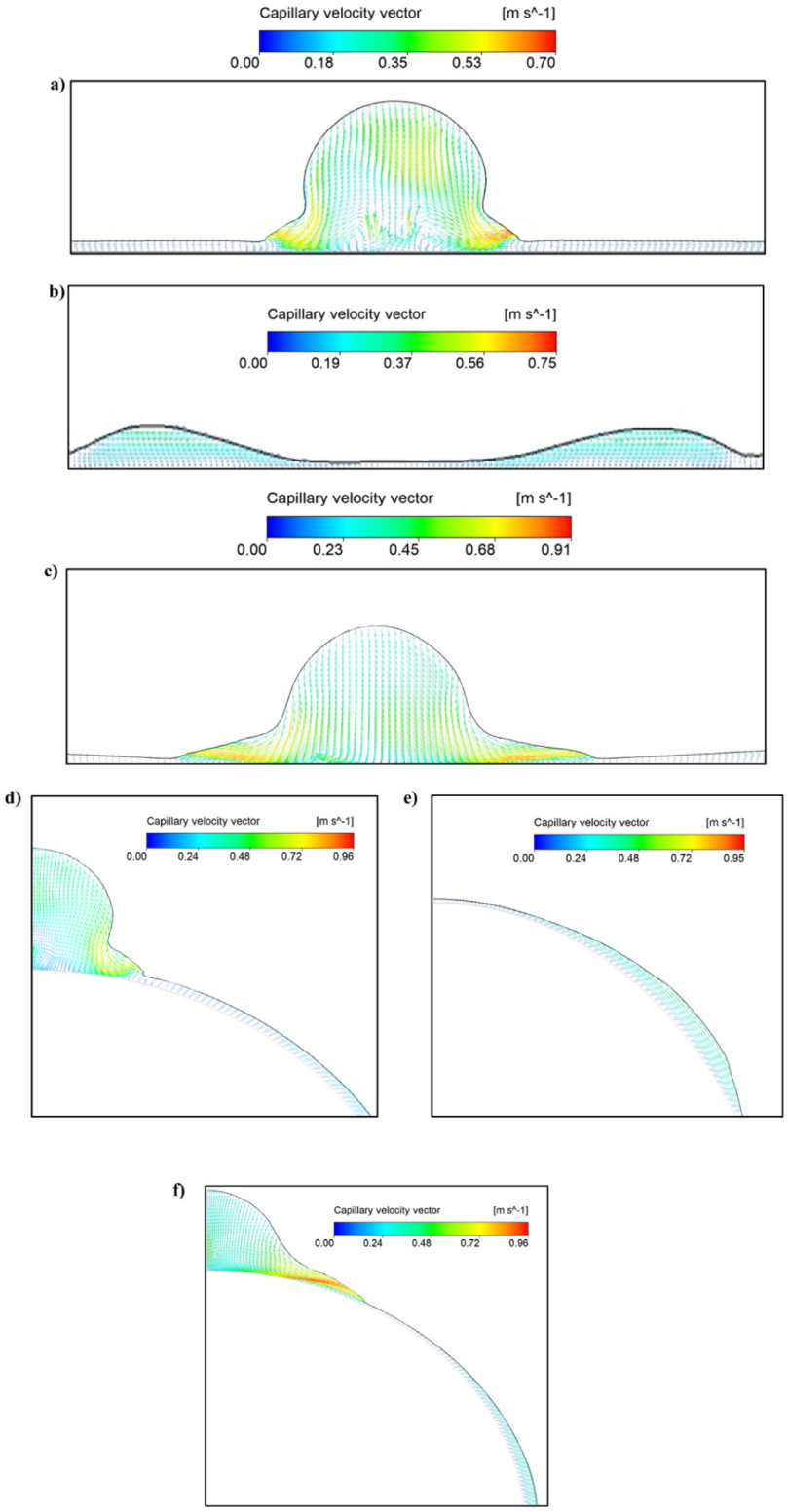

Fig. 10. Velocity vector plot of the liquid film impacting the middle of the second tube (from 30 to 50 ms) in the axial (a-c) and circumferential directions (d-f).

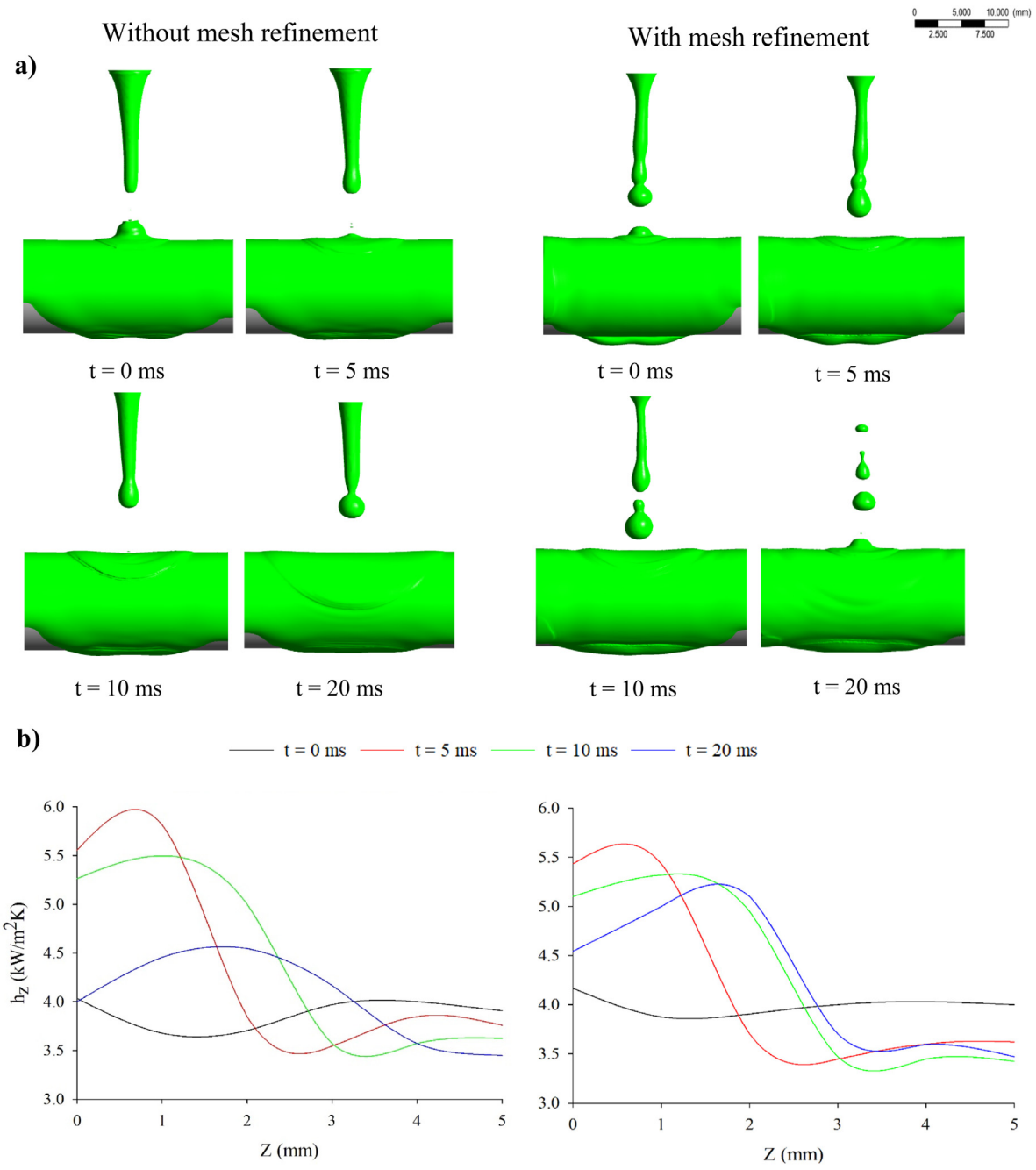

Fig. 11. a) Jet instability behaviour with and without mesh refinement on the second tube just after satellite droplet impaction. b) Axial heat transfer coefficient within the liquid film where Z = 0 mm is taken from the centre of droplet impaction.

wards the bottom of the tube where they constructively interfere with the nucleating droplet and affect the morphology and departure rate of the droplets. The increased number of waves generated due to the further number of satellite droplets captured will increase the disturbance of the droplet causing it to depart faster than if the Rayleigh instability was not captured. It is noteworthy that these capillary waves have been displayed to promote film mixing and thinning which further increase the heat and mass transfer rates in conventional absorption systems [8,35-38]. However, the magnitude of wave velocity starts to slow as the subsequent droplets impact the film (seen in Fig. 9) due to their hydrostatic pressure being smaller than the other (size of the droplets declines).

The film mixing phenomenon within the fluid can be seen in Fig. 10 from the velocity vector fields in the axial and circumferential directions on the second tube. In Fig. 10 (a and d), initially as the satellite droplet impacts the film, the velocity vector field within the film shows little or no movement in the bulk region of the film. In the vicinity of droplet impaction, the capillary velocity begins to increase as the generated saddle wave spreads across the film in all directions. Whilst the wave spreads, the wave dynamically creates regions of high and low pressures (seen from the squashed regions of the fluid) which enhances the flow of the liquid as shown in Fig. 10 (b-c, e-f).

To illustrate how film mixing can alter the local heat transfer rate, Fig. 11 shows the axial local heat transfer coefficient within the liquid film just after the first satellite droplet impacts the film which is compared before (Fig. 11a) and after the Rayleigh instability improvement (Fig. 11b). At 0 ms, the local heat transfer coefficient is lower within the droplet impaction regime in both cases

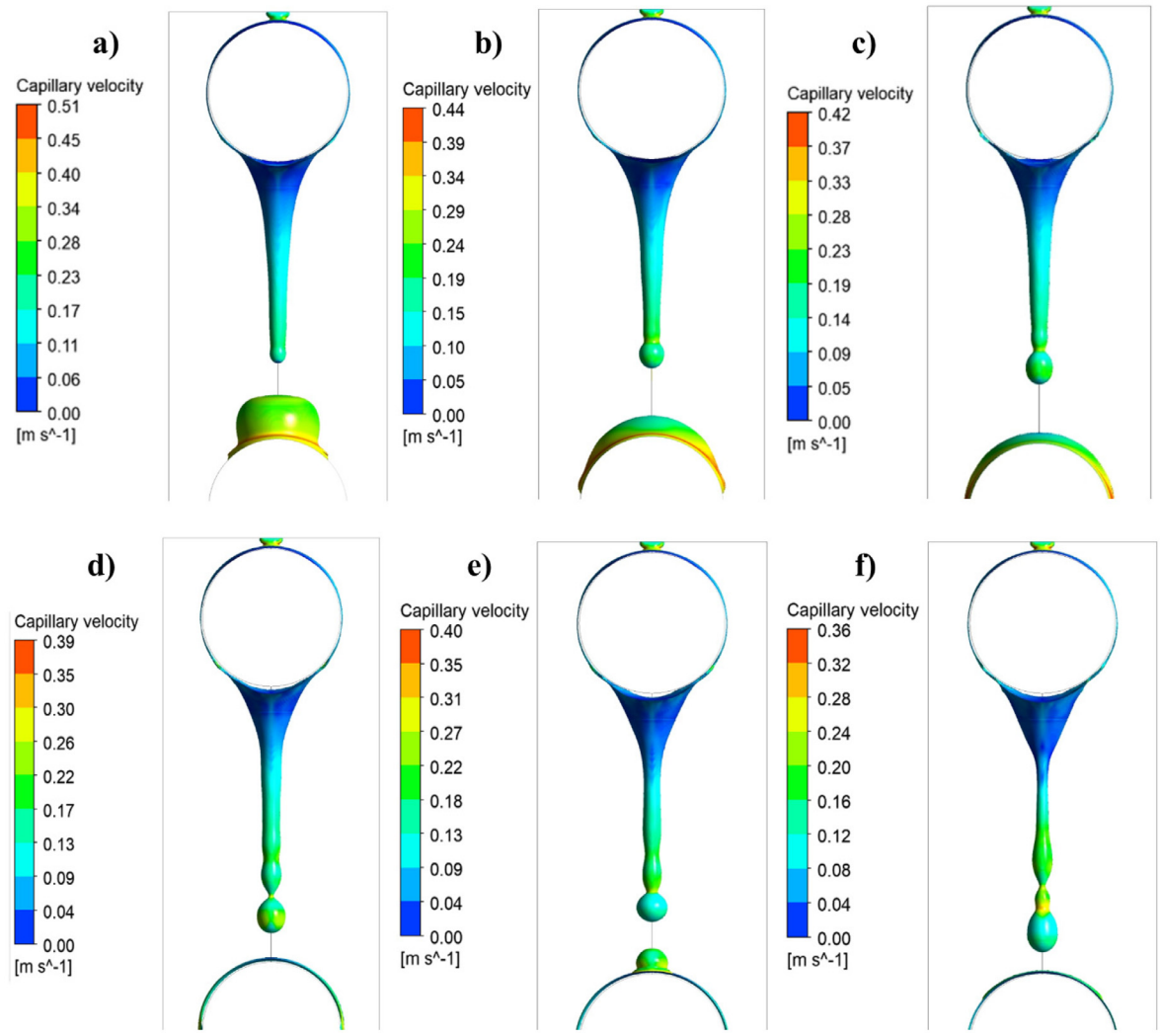

Fig. 12. Velocity contours of first droplet impaction onto second tube following on to Rayleigh-Plateau instability.

compared to the rest of the tube. This is due to the increased film thickness which is found to be inversely proportional to the local heat transfer rate [28,39]. As the droplet flattens into a saddle wave (5 ms), the liquid film within intermediate region begins to thin, which amplifies the local heat transfer coefficient causing the liquid film to cool. Between 5 to 10 ms, the capillary wave continues to spread across the tube which is seen in both graphs as the maxima point of the wave shifts axially along the tube. However, at the same time, the heat transfer coefficient declines as the saddle wave begins to settle within the film. Notably, for the improved Rayleigh capture state, another satellite droplet is detached from the ligament, whilst for the flow state without mesh refinement, the jet is still formulating a satellite droplet. At 20 ms, for the mesh refinement state, the satellite droplet impacts the tube, generating another capillary wave with the rest of the jet being broken into multiple satellite droplets. This promptly increases the local heat transfer coefficient as shown previously when the first satellite droplet impacted the film. For the flow state without mesh refinement, the heat transfer coefficient continues to decline as the capillary wave travels further along the tube with a second satellite droplet just beginning to be detached. This demonstrates how the additional capillary waves generated from the satellite droplets can enhance the local heat transfer rate by promoting film mixing, thinning and cooling.

To explore the mechanism of the Rayleigh-Plateau instability, Fig. 12 demonstrates the velocity contours of the jet just after the ligament breaks away from the leading droplet whilst Fig. 13 depicts the axial velocity and pressure variation within the liquid jet. In Fig. 12a/Fig. 13a, the tip of the liquid jet contracts away from the droplet as the interfacial tension force starts to overcome the viscous forces. As doing so, capillary waves begin to generate at the apex of the formulating satellite droplet. As a consequence, the axial pressure gradient begins to fluctuate around the droplet and decrease towards the bulk region of the jet according to the Young-Laplace equation [40,41]:

$$\Delta p = \frac{2\gamma_{lg}}{r_j} \tag{37}$$

where r_j is the radius of the jet. The capillary waves then start to propagate parallel to the direction of recoil (caused by capillary tension) in the form of a harmonic sinusoidal wave (Fig. 12b) and disperses its kinetic energy. Subsequently, the axial velocity falls and inversely increases the amplitude of the pressure gradient along the necked region of the jet but then suddenly increases once reaching towards the undisturbed region of the jet (Fig. 12b). Due to the harmonic oscillations subsided from the capillary wave, the interface of the jet is perturbated. As a result, the interfacial surface tension starts to become unbalanced and takes the harmonic form of the generated capillary wave. Notably, more subsequent satellite droplets form from the unstable jet as the capillary waves further travel up the jet as displayed in Fig. 12c/Fig. 13c. The formation of these droplets is due to the change in the sinu-

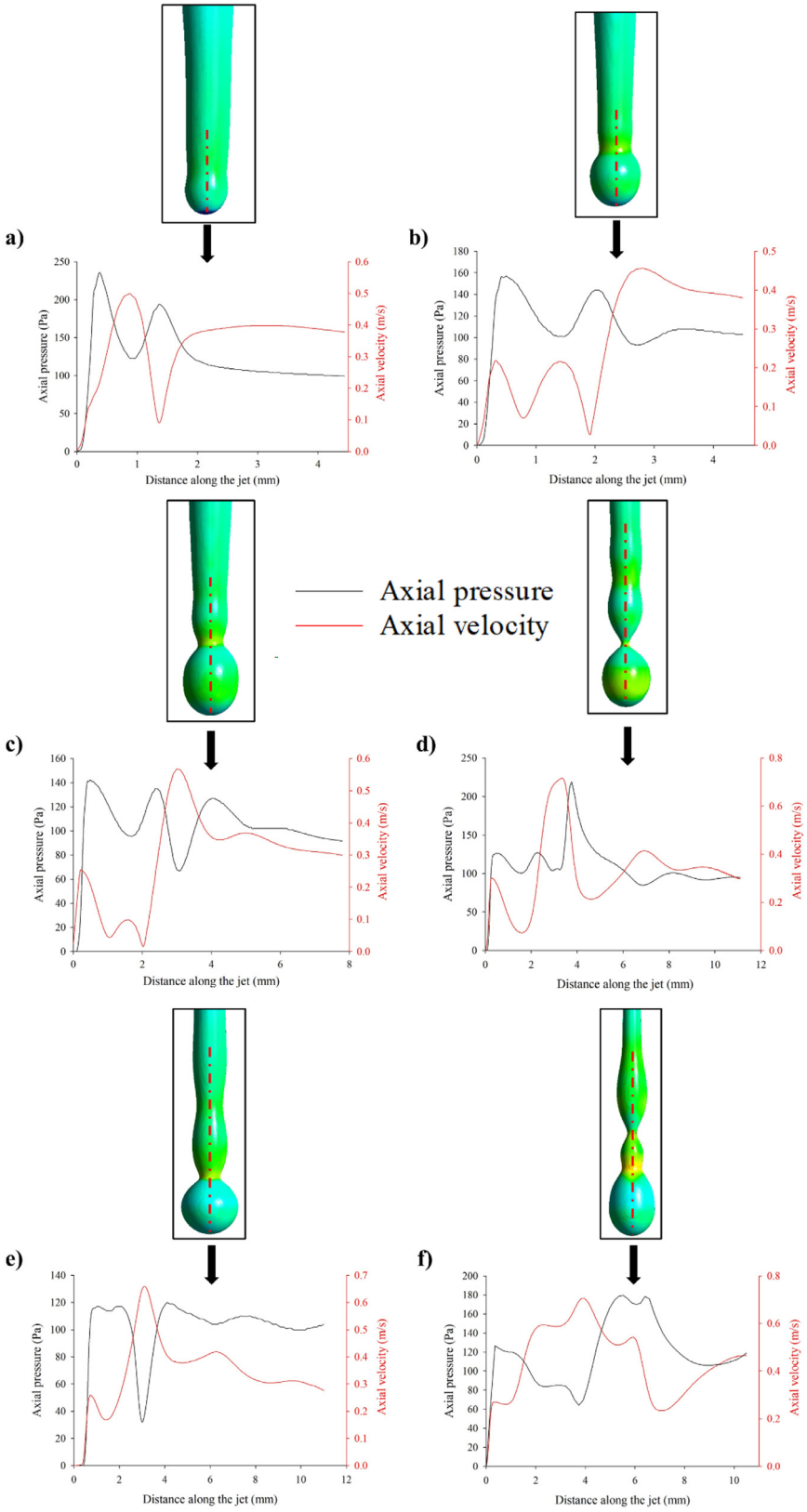

Fig. 13. Axial velocity and pressure fluctuations within the central region of the unstable jet over time.

soidal Laplace pressure gradient along its local maxima and minima points, which create regions of convex and concave curvatures along the jet. These observations coincide well with previously reported results for axial pressure variations [42]. Interestingly, the axial velocity starts to increase in magnitude near towards the necked regions of the jet. This is due to the amplitude of the capillary wave being high, which causes the surface tension force (along the convex regions) to become dominant over the concave regions [43]. Therefore, the axial velocity of capillary waves is dependent upon the wavelength [42]. This can be shown in Fig. 13c onwards where the wavelength appears to be longer within the bulk region of the jet also having a smaller amplitude.

In Fig. 12d/Fig. 13d and beyond, the satellite droplets begin to detach from the liquid filament as the jet starts to become thinner due to capillary tension which pulls the jet towards the tube. Therefore, the diameter of the jet starts to decline which further increases the Rayleigh instability as the capillary wavelength can surpass the lowered jet diameter.

3.3. Falling-film flow behaviour at different contact angles

To briefly describe the flow behaviour on a completely wetted tube (contact angle of 0°), as shown in Figure S1a and Supplementary Movie 1, when exiting out of the inlet feeder, it is noted that the liquid spreads rapidly to form a thin film around the entity of the tube. Due to the inertia force provided by the feeder and gravitational force acting in the direction of the flow, the liquid is accelerated towards the bottom of the tube where a droplet begins to nucleate. Once the hydrostatic pressure (gravitational force) is able to overcome the surface tension, the droplet departs and impacts the second tube where it also fully wets the surface. The same can be found on the third tube as well. Noticeably, just after 0.8 s, the droplet nucleation site has slightly shifted towards the left. This is mainly due to the Taylor wavelength instability where the amplitude of the wavelength changes as the liquid jet is recoiled back to the tube. The recoil velocity directly affects the interfacial surface tension forces, which alters the growth rate of the wave amplitude hence increasing the instability of the droplet formation site [8,44,45].

For a tube contact angle of 30° the falling-film mode illustrates a dropwise flow (shown in Figure S1b and Supplementary Movie 2) by resolving the Rayleigh instability. This is shown from the small successive satellite droplets that form from the liquid jet as the jet recoils back to the tube after droplet impaction (seen at $t \geq 0.4$ s). In comparison to the work by Ding *et al.*, the flow shows a laminar liquid jet throughout with no sign of jet instability or satellite droplets [18]. Notably, the spreading of the liquid along the first tube is substantially smaller than that of a tube with a contact angle of zero degree. It forms a circumferential ring around the centre of the tube where its axial thickness near the top of the tube is larger than the bottom (shown from $t \geq 0.2$ s). The reason is due to the reduced surface adhesion force the fluid experiences which causes the inertia, surface tension and gravitational force experienced by the feeder to become highly dominant. This prevents the liquid from spreading more axially than circumferentially as the surface tension force is able to overcome the viscous force at a smaller axial distance [46]. The point where the liquid no longer spreads axially on the tube is where the surface tension and viscous forces balance. This effect is particularly evident at larger contact angles. Since the surface tension force withdraws the liquid towards the centre of the tube, the film thickness starts to increase, which creates a rise in the hydrostatic pressure hence increasing the film flow rate.

As the fluid flows in the circumferential direction, a droplet swiftly forms and starts to depart from the tube at $t = 0.2$ s. Since the surface adhesion force is reduced, the gravitational force is able to overwhelm the surface tension at a smaller magnitude therefore increasing the droplet departure rate. The same can be found on the tubes beneath where the spreading area of the liquid has decreased causing the liquid to rapidly be removed off the surface whilst still being in dropwise mode (for the second and third tubes). The formation of the sequential satellite droplets that impact the film is what causes the flow to be dropwise since the film thickness is unable to reach a steady state value, hence, increasing film instability [11]. At a contact angle of 60° (Figure S1c and Supplementary Movie 3), the flow is primarily in a dropwise/jet flow state due to the increased surface tension force and the Rayleigh instability capture as explained previously.

These observations are valid up to a critical contact angle of 90° where the flow no longer exhibits a falling-film manner as seen in Figure S1d and Supplementary Movie 4. At this point, the surface tension force has become so prevalent that the liquid film breaks into two droplets (formed on either side of the tube) before reaching the bottom of the tube when $t \geq 0.16$ s. The droplets then start to detach towards the bottom of the tube with a thin liquid film still being attached onto the tube. As the droplets wet the tubes beneath, macroscopic droplets are formed on the surface with some being restored to a hemispherical shape. This indi-

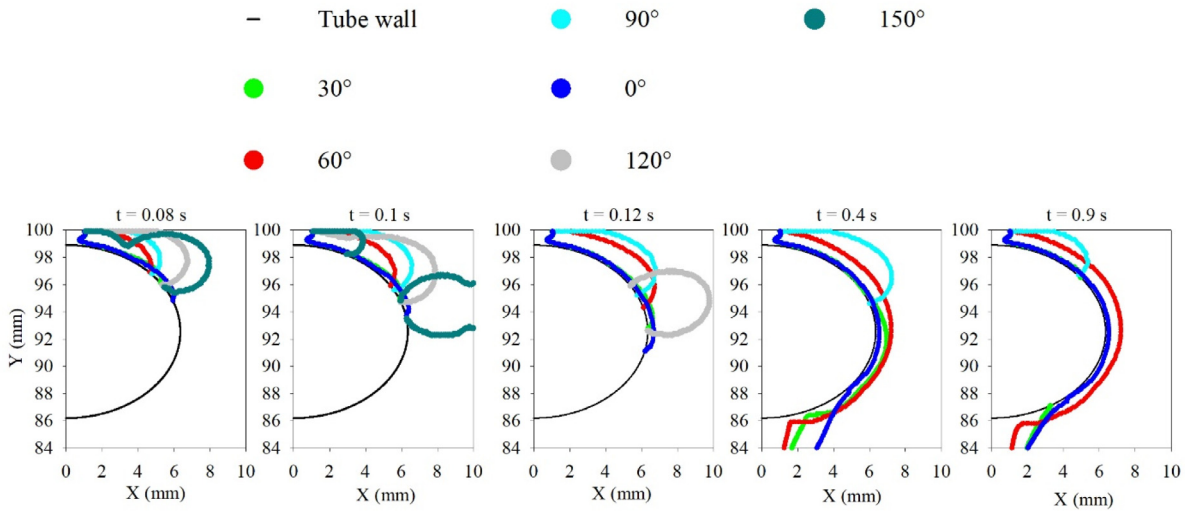

Fig. 14. Contour plots of the flow behaviour around the first tube at multiple contact angles.

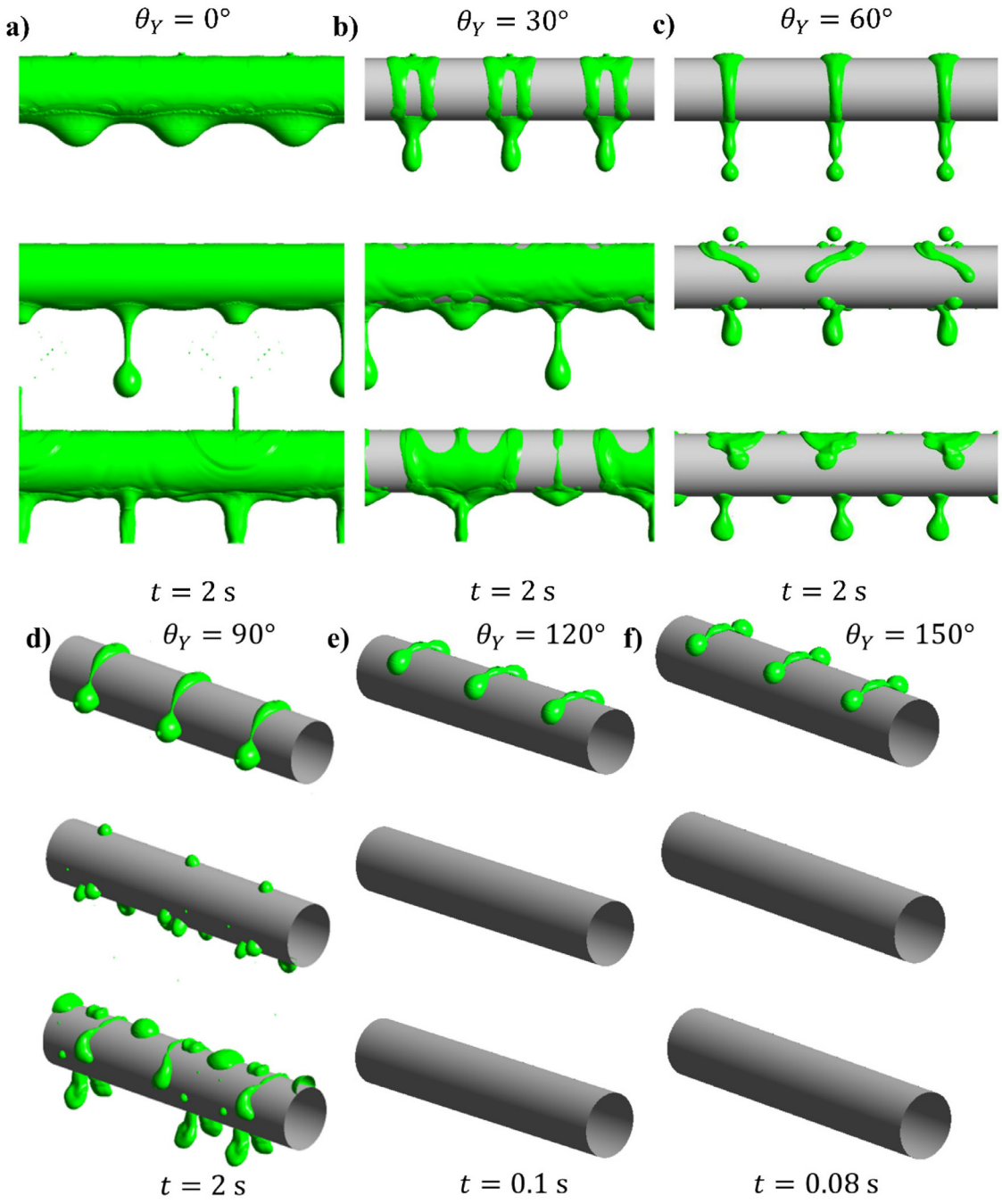

Fig. 15. Hydrodynamic flow of liquid falling over the configurated pipes at different static contact angle states namely (a) 0°, (b) 30°, (c) 60°, (d) 90°, (e) 120° and (f) 150°.

cates that the adhesion force of the surface has minimised to the point where the surface tension force is beginning to overcome the inertia force generated from droplet impact. Nevertheless, at even larger contact angles from 120 to 150°, (Figure S1e-f and Supplementary Movies 5-6) droplets no longer impact the tubes beneath but roll off the first tube and escape the fluid domain. Due to the amply reduced surface adhesion force, the tangential component of the gravitational force and surface tension force have become large enough to cause the droplet to depart from the tube at a relatively small circumferential angle [47].

In the early stages of film formation (when t = 0.08 s), as the contact angle of the tubes increases, the film thickness along the circumferential direction begins to thicken. This is because the amplified surface tension force pulls the liquid towards the feeder. By 0.1 s, for a contact angle of 150°, the droplet has already detached itself from the liquid film and has begun to leave the tube. At 0.12 s, the droplet has completely left the tube and the fluid domain leaving the tube completely bare as doing so. This flow behaviour described simply repeats itself every 0.12 s. Notably at the same time for 120°, a droplet is formed and is separated from the film. When t = 0.4 s, the film has mostly covered the entirety of the first tube for contact angles of 0, 30 and 60°. Clearly at this stage, the film thickness is shown to rise between 0 and 60° (Fig. 14), which has been explained earlier.

Particularly at 60°, the film has already separated itself from the second tube whereas for 30°, the film is just beginning to expand along the tube. At 0°, the film is still developing to initiate droplet nucleation. The film flow for 0° ultimately starts to catch up to the other contact angles when t = 0.6 s where the droplet has already impacted the second tube and the jet has been broken

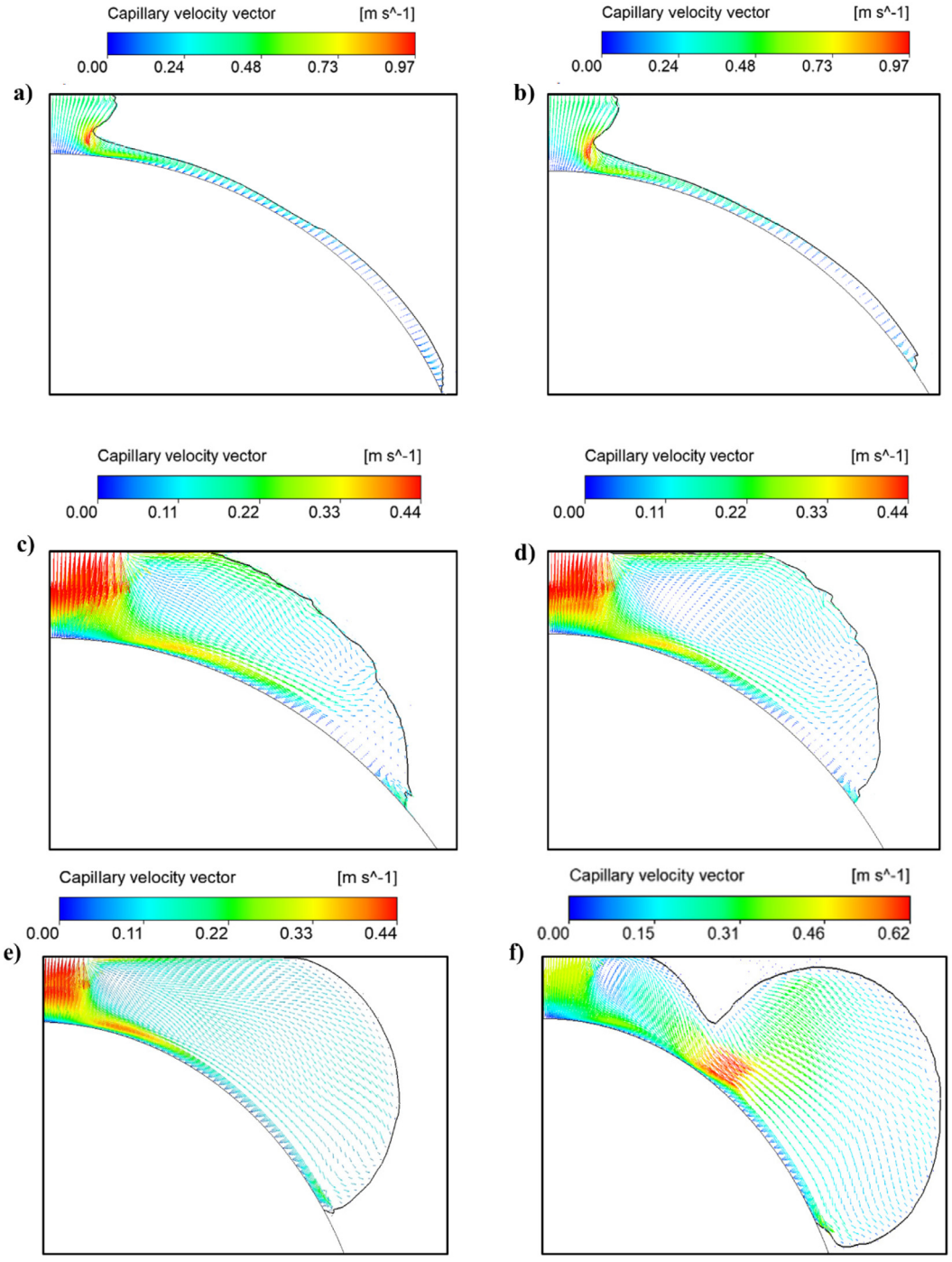

Fig. 16. Velocity vector plot of the fluid exiting the inlet in the circumferential direction at different contact angles when t = 0.08 s. (a) 0° (b) 30° (c) 60° (d) 90° (e) 120° (f) 150°.

into small satellite droplets. Remarkably, at t = 0.9 s for a contact angle of 30°, the film in the circumferential direction splits in the middle and is divided axially. However, the flow behaviour still remains dropwise. Finally, when t = 2 s the final state of the flow pattern is revealed for each contact angle in Fig. 15. For 0°, the flow remains dropwise. At 30° and 60° the flow pattern indicates a consistent dropwise and dropwise/jet flow up to 2 s. As for 90°, the flow does not follow a falling-film behaviour, and there are just continuous droplets that migrate off the tubes. The same is applicable for 120° and 150°, although the droplets do not interact with the tubes beneath as stated before.

Figure 16 illustrates the velocity vector plot of the fluid flow within the liquid at different contact angles when t = 0.08 s. Initially, for contact angles of 0° and 30°, the velocity is relatively large at the necking region due to the reduction in the fluids' surface area. However, within the bulk region, the velocity of flow is reduced from the effects of increased surface adhesion. At larger contact angles, the velocity at the inlet region appears to be approximately the same as the prescribed velocity inlet since the interface of the fluid is undisturbed. Nevertheless, due to the growth in the circumferential film thickness between the contact angles, the velocity gradient of the fluid begins to increase. Most of the

fluid is retained in the circumferential direction rather than the axial direction causing an increase of the inertial force, although, at the contact angle of 150°, the velocity begins to increase again due to the reduced surface area, which causes the droplet to be swiftly removed off the tube in comparison to lower contact angles.

4. Conclusion

Numerical simulations capturing the Rayleigh-Plateau instability of liquid jets have been performed in this work by refining the mesh where the liquid jet is propelled. The fluid dynamics of the flow has been successfully verified against previously published experimental results on the first and second tubes alongside the axial and circumferential capillary waves. Additionally, the film thickness, velocity profiles, average and local heat transfer coefficients across the first tube were reasonably calibrated against numerical solutions. A suitably resolved Rayleigh-Plateau instability has also been verified against previous results for axial pressure variations within an unstable liquid jet. Furthermore, the hydrodynamics of the flow pattern at different contact angles have been investigated and scrutinized. The following aspects of this investigation are summarised as follows:

- Increasing the Rayleigh instability capture causes more satellite droplets to form towards the expected amount seen in experimental results as the jet recoils back to the tube. This further increases the number of capillary waves seen on the impacted tube as each individual droplet increases the film waviness and instability. As a result, the local heat transfer coefficient is also increased due to the sudden reduction in film thickness. The enhanced film instability causes the film to be abruptly removed off the tube, affecting droplet departure rates and droplet nucleation.
- Axial pressure capillary wave variations within the liquid jet displays a sinusoidal profile during jet contraction. This is what causes the Rayleigh-Plateau instability to occur, due to increased Laplace pressure gradient inflicted by the restored surface tension force. The points of minima and maxima inflexion seen on the axial pressure profile indicate the necking regions of the liquid jet which eventually forms satellite droplets. The change in the axial velocity is associated with the variation in the capillary wavelength along the jet.
- Increasing the contact angle of the tubes causes the film thickness along the circumferential direction to promptly rise with the axial film thickness being substantially smaller. It should be noted that, only contact angles of 0°, 30° and 60° lead to a falling-film flow. For the contact angle of 90°, the flow shows no falling-film effects but constant removal of macroscopic droplets that impact the tube beneath. At even higher contact angles up to a superhydrophobic state, the formulated droplets simply roll off the fluid domain.
- For a contact angle of 30° and 60°, by introducing the Rayleigh instability capture, the falling film pattern has constantly remained to be in a dropwise and dropwise/jet state throughout the 2 seconds simulated.

Future studies on falling films should extend the analyses under real industrial environments such as the effect of laminar or turbulent vapour flow orthogonal to the pipes, implementing dynamic contact angles and including vapour properties at saturated conditions. Multiple adjacent tube banks could be simulated for highly hydrophobic tubes (contact angles more than 120°) as the droplets that depart off the tube could interact with adjacent tubes beneath or on the first tube. Most importantly, the Rayleigh-Plateau instability should be carefully considered in relation to falling films, since this phenomenon will determine whether the flow pattern is either jet or dropwise/jet as examined here which will have implications on the wetting phenomena of the tubes beneath. Additionally, this will affect the heat and mass transfer characteristics of the tube as the enhanced film waviness promoted from the numerous satellite droplets will increase the rate of convection and mass transfer within the film. Likewise, this allows numerical flow patterns to be directly compared against experimental observations for different tube contact angles.

Declaration of competing interest

The authors declare no conflict of interest.

Data availability

Data will be made available on request.

Acknowledgements

We would like to thank the School of Engineering, University of Birmingham for supporting this work. Additionally, the numerical work presented was accomplished using the University of Birmingham's BlueBEAR HPC (high performance computing) service, which allows the University's academics to undertake more computationally challenging work. For more information, visit http://www.birmingham.ac.uk/bear.

Supplementary materials

Supplementary material associated with this article can be found, in the online version, at doi:10.1016/j.ijheatmasstransfer.2023.123936.

References

[1] D. Popov, K. Fikiin, B. Stankov, G. Alvarez, M. Youbi-Idrissi, A. Damas, J. Evans, T. Brown, Cryogenic heat exchangers for process cooling and renewable energy storage: a review, Appl. Therm. Eng. 153 (2019) 275–290.
[2] A. Stärk, K. Krömer, K. Loisel, K. Odiot, S. Nied, H. Glade, Impact of tube surface properties on crystallization fouling in falling film evaporators for seawater desalination, Heat Transfer Eng. 38 (2017) 762–774.
[3] A. Austegard, M. Bandopadhyay, S.W. Løvseth, A. Brunsvold, Flow pattern transitions in and hysteresis effects of falling film flow over horizontal tubes related to LNG heat exchangers, Energy Procedia 64 (2015) 23–32.
[4] Y. Zhang, M.T. Munir, I. Udugama, W. Yu, B.R. Young, Modelling of a milk powder falling film evaporator for predicting process trends and comparison of energy consumption, J. Food Eng. 225 (2018) 26–33.
[5] I. Kyung, K.E. Herold, Y.T. Kang, Model for absorption of water vapor into aqueous LiBr flowing over a horizontal smooth tube, Int. J. Refrig. 30 (2007) 591–600.
[6] X.Ma Y.Zheng, Y. Liu, R. Jiang, K. Wang, Z. Lan, Q. Liang, Experimental study of falling film evaporation heat transfer on superhydrophilic horizontal-tubes at low spray density, Appl. Therm. Eng. 111 (2017) 1548–1556.
[7] X. Hu, A.M. Jacobi, The intertube falling film: Part 1—flow characteristics, mode transitions, and hysteresis, Trans. Am. Soc. Mech. Eng. J. Heat Transfer. 118 (1996) 616–625.
[8] J.D. Killion, S. Garimella, Gravity-driven flow of liquid films and droplets in horizontal tube banks, Int. J. Refrig. 26 (2003) 516–526.
[9] J. Eggers, E. Villermaux, Physics of liquid jets, Rep. Prog. Phys. 71 (2008) 036601.
[10] S.D. Hoath, Fundamentals of Inkjet Printing: The Science of Inkjet and Droplets, JWS (2016) 93–115.
[11] W. Van Hoeve, S. Gekle, J.H. Snoeijer, M. Versluis, M.P. Brenner, D. Lohse, Breakup of diminutive Rayleigh jets, Phys. Fluids 22 (2010) 122003.
[12] F. Gallaire, P.T. Brun, Fluid dynamic instabilities: theory and application to pattern forming in complex media, Philos. Trans. R. Soc. London, Ser. A 375 (2017) 20160155.
[13] L. Rayleigh, On the capillary phenomena of jets, Proc. R. Soc. London 29 (1879) 71–97.
[14] K. Graessel, C. Bächer, S. Gekle, Rayleigh–Plateau instability of anisotropic interfaces. Part 1. An analytical and numerical study of fluid interfaces, J. Fluid Mech. 910 (2021).
[15] R. Mead-Hunter, A.J. King, B.J. Mullins, Plateau Rayleigh instability simulation, Langmuir 28 (2012) 6731–6735.
[16] G.H. Mckinley, Dimensionless groups for understanding free surface flows of complex fluids, (2005) 1-8.

[17] S.S. Deshpande, L. Anumolu, M.F. Trujillo, Evaluating the performance of the two-phase flow solver interFoam, Comput. Sci. Discov. 5 (2012) 014016.
[18] H. Ding, P. Xie, D. Ingham, L. Ma, M. Pourkashanian, Flow behaviour of drop and jet modes of a laminar falling film on horizontal tubes, Int. J. Heat Mass Transfer 124 (2018) 929–942.
[19] J. Shinjo, A. Umemura, Simulation of liquid jet primary breakup: dynamics of ligament and droplet formation, Int. J. Multiphase Flow 36 (2010) 513–532.
[20] S.M. Hosseinnia, M. Naghashzadegan, R. Kouhikamali, CFD simulation of water vapor absorption in laminar falling film solution of water-LiBr – drop and jet modes, Appl. Therm. Eng. 115 (2017) 860–873.
[21] Y. Thomas, An essay on the cohesion of fluids, Philos. Trans. R. Soc. London 95 (1805) 65–87.
[22] K.Y. Law, Definitions for hydrophilicity, hydrophobicity, and Superhydrophobicity: getting the Basics Right, J. Phys. Chem. Lett. 5 (2014) 686–688.
[23] D. Bonn, J. Eggers, J. Indekeu, J. Meunier, E. Rolley, Wetting and spreading, Rev. Mod. Phys. 81 (2009) 740–793.
[24] B. Köroğlu, K.S. Lee, C. Park, Nano/micro-scale surface modifications using copper oxidation for enhancement of surface wetting and falling-film heat transfer, Int. J. Heat Mass Transfer 62 (2013) 794–804.
[25] N. Miljkovic, R. Enright, Y. Nam, K. Lopez, N. Dou, J. Sack, E.N. Wang, Jumping–droplet-enhanced condensation on scalable superhydrophobic nanostructured surfaces, Nano Lett. 13 (2013) 179–187.
[26] T.Y. Zhang, L.W. Mou, J.Y. Zhang, L.W. Fan, J.Q. Li, A visualized study of enhanced steam condensation heat transfer on a honeycomb-like microporous superhydrophobic surface in the presence of a non-condensable gas, Int. J. Heat Mass Transfer 150 (2020) 119352.
[27] R. Armbruster, J. Mitrovic, Heat transfer in falling film on a horizontal tube, Trans. Am. Soc. Mech. Eng. (1995) 13–21.
[28] A. Karmakar, S. Acharya, Numerical simulation of falling film sensible heat transfer over round horizontal tubes, Int. J. Heat Mass Transfer 190 (2022) 122727.
[29] J.U. Brackbill, D.B. Kothe, C. Zemach, A continuum method for modeling surface tension, J. Comput. Phys. 100 (1992) 335–354.
[30] R. Courant, K. Friedrichs, H. Lewy, On the partial difference equations of mathematical physics, IBM J. Res. Dev. 11 (1967) 215–234.
[31] D.L. Youngs, Numerical methods for fluid dynamics, Time-dependent multi–material flow with large fluid distortion, AP (1982) 273–285.
[32] R.B. Bird, W.E. Stewart, E.N. Lightfoot, Transport phenomena, JWS 1 (2006) 40–74.
[33] J. Rogers, Laminar falling film flow and heat transfer characteristics on horizontal tubes, Can. J. Chem. Eng. 59 (1981) 213–222.
[34] S. Inada, Y. Miyasaka, R. Izumi, A study on the laminar-flow heat transfer between a two-dimensional water jet and a flat surface with constant heat flux, Bull. JSME 24 (1981) 1803–1810.
[35] V. Patnaik, H. Perez-Blanco, A study of absorption enhancement by wavy film flows, Int. J. Heat Fluid Flow 17 (1996) 71–77.
[36] S. Jayanti, G. Hewitt, Hydrodynamics and heat transfer of wavy thin film flow, Int. J. Heat Mass Transfer 40 (1996) 179–190.
[37] I. Mudawar, R.A. Houpt, Measurement of mass and momentum transport in wavy-laminar falling liquid films, Int. J. Heat Mass Transfer 36 (1993) 4151–4162.
[38] R. Collignon, O. Caballina, F. Lemoine, C.N. Markides, G. Castanet, Heat transfer enhancement in wavy falling films studied by laser-induced fluorescence, Int. J. Heat Mass Transfer 202 (2023) 123690.
[39] C.-Y. Zhao, D. Qi, W.-T. Ji, P.-H. Jin, W.-Q. Tao, A comprehensive review on computational studies of falling film hydrodynamics and heat transfer on the horizontal tube and tube bundle, Appl. Therm. Eng. 202 (2022) 117869.
[40] J. Pellicer, V. Garcia-Morales, M. Hernandez, On the demonstration of the Young-Laplace equation in introductory physics courses, Phys. Educ. 35 (2000) 126.
[41] B.E. Rapp, Chapter 23 - plateau-rayleigh instability, in: B.E. Rapp (Ed.), Microfluidics: Modelling, Mechanics and Mathematics, Elsevier, 2017, pp. 467–477.
[42] A. Umemura, Self-destabilizing mechanism of a laminar inviscid liquid jet issuing from a circular nozzle, Phys. Rev. E 83 (2011) 046307.
[43] A. Karmakar, S. Acharya, Numerical simulation of falling film flow hydrodynamics over round horizontal tubes, Int. J. Heat Mass Transfer 173 (2021) 121175.
[44] R. Bellman, R.H. Pennington, Effects of surface tension and viscosity on Taylor instability, Q. Appl. Math. 12 (1954) 151–162.
[45] N. El-Ansary, G. Hoshoudy, A. Abd-Elrady, A. Ayyad, Effects of surface tension and rotation on the Rayleigh–Taylor instability, Phys. Chem. Chem. Phys. 4 (2002) 1464–1470.
[46] C. Cao, L. Xie, X. He, Q. Ji, H. Zhao, Y. Du, Numerical study on the flow and heat-transfer characteristics of horizontal finned-tube falling-film evaporation: Effects of liquid column spacing and wettability, Int. J. Heat Mass Transfer 188 (2022) 122665.
[47] F. Tahir, A. Mabrouk, M. Koc, Review on CFD analysis of horizontal falling film evaporators in multi effect desalination plants, Desalin. Water Treat 166 (2019) 296–320.